Part VII
Fiber Fuse Effect in Hollow-Core Photonic Crystal Fibers

1 Hollow-Core Photonic Crystal Fibers

Hollow-core photonic crystal fibers (HC-PCFs) can guide light inside the hollow core by photonic bandgap (PBG) [1] or inhibited-coupling (IC) mechanisms [2]. The confinement loss in IC-guiding HC-PCFs, represented by kagome-lattice HC-PCFs [3], has been reduced from the 1 dB/m level to 8.5–70 dB/km with the introduction of a fiber core with a hypocycloid-like shape [4]–[7]. The role of the hypocycloid shape in decreasing the confinement loss was explained by an enhancement of IC via a dramatic decrease in the spatial overlap between the slow-varying transverse-phase core modes and the fast-varying transverse cladding modes [8], [9].

Furthermore, the relationship between the negative curvature and the confinement loss in the HC-PCF family has been experimentally and theoretically investigated by several research institutes [10]–[30]. Pryamikov *et al.* fabricated a novel hollow-core PCF with a negative curvature of the core boundary and a cladding consisting of one row of capillaries [10]. This fiber is often called an antiresonant fiber [14], [15], [20], [25], [28], a negative curvature fiber [11]–[13], [19], [21], [23], or a revolver fiber [18], [24]. Recently, Sakr *et al.* reported the fabrication of the nested antiresonant nodeless hollow-core fiber (NANF) with a record low loss of 0.51 dB/km at 1.064 μm [29] and Jasion *et al.* reported the minimum loss of 0.28 dB/km between 1.51 and 1.60 μm in the NANF [30].

The HC-PCFs can provide a large light-gas interaction overlap inside hollow-core [31], [32] and wide transmission bands [33], exhibiting the potential for improving gas detection performance [34] and realizing a high-performance gas fiber laser [35]–[42]. On the other hand, the use of high-power lasers in the industry has been rapidly advanced by incorporating flexible-fiber-based beam delivery. The high-power laser beams cannot be transported through traditional step-index fibers as their peak intensity lies above the damage threshold of silica and would therefore destroy the fiber itself. The HC-PCFs are now implemented as a tool of laser beam delivery in place of traditional optical fibers [43]–[49].

The fiber fuse effect in kagome-lattice HC-PCFs [46] and revolver fibers [50], [51] has been reported. In this chapter, we investigated the generation of a fiber fuse and its propagation in kagome-lattice HC-PCFs and revolver fibers by the explicit finite-difference method using the thermochemical SiO_x production model.

2 Kagome-Lattice HC-PCF

The occurrence of the fiber fuse in a kagome-lattice HC-PCF was first reported in 2014 by Dumitrache *et al.* [46]. They conducted high-power laser pulse delivery experiments using kagome-lattice HC-PCFs with a core diameter of 50 μm [4].

A schematic illustration of the fiber is shown in Fig. 1. In this figure, r_c (=

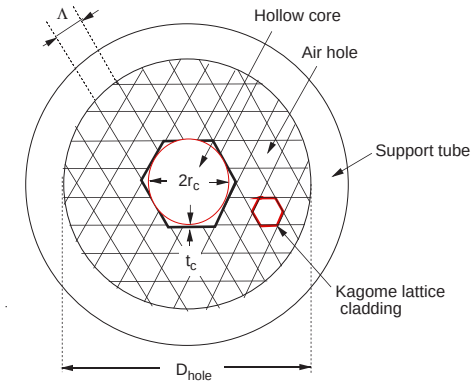

Figure 1: Schematic illustration of kagome-lattice HC-PCF.

25 μm) and D_{hole} ($\sim$164 μm) are the radius of the hollow core and the outer diameter of the kagome lattice cladding, respectively, and t_c (= 0.28 μm) is the thickness of a silica strut of the kagome lattice. The fiber was first flushed with neon to remove any trapped dust inside the fiber (hollow) core [43].

2.1 Surface Damage at Fiber Tip

Dumitrache *et al.* were able to transmit as much as 30 mJ of energy through the fiber for 30 ns pulses at 1.064 μm [46]. The focused diameter of the fiber input was 41 μm. However, damage occurred on the fiber tip when the input energy was increased to 35 mJ, and it propagated inward at a rate of about 0.0003 m/s when the laser was not immediately turned off.

Laser-induced breakdown can be identified by the formation of an ionized gas or plasma during or by the end of the laser pulse [52]. When employing high-power pulses, the breakdown threshold intensity I_B for air at the focal minimum is determined by [52]

$$I_B = \frac{1}{\pi}\left(\frac{W_B}{r_0^2 \tau_p}\right), \tag{1}$$

where W_B is the minimum laser pulse energy at which the breakdown is observed, r_0 is the focal spot radius, and τ_p is the duration or the full width at

half-maximum (FWHM) of the laser pulse. The I_B for air was estimated to be 8.8 $\times 10^{10}$ W/cm^2 when using W_B = 35 mJ, r_0 = 20.5 μm, and τ_p = 30 ns. This value is close to the experimentally determined I_B (8.2 $\times 10^{10}$ W/cm^2 [53]). When the input energy of the laser radiation in the focal region becomes greater than the excitation energy for air, it will trigger breakdown of air molecules and cause ionization. In this initial breakdown (multiphoton ionization) process, a neutral atom absorbs enough laser photons to raise it from the ground state to the ionization level or above. Following the multiphoton ionization (MPI) process, the cascade effect takes place owing to the increased plasma density and the medium becomes opaque to the laser beam, leading to further energy absorption. This cascade ionization (CI) process produces a very sudden temperature rise in the medium at the focal region and results in the complete destruction of the internal structure of the fiber tip, as observed by Dumitrache *et al.* [46].

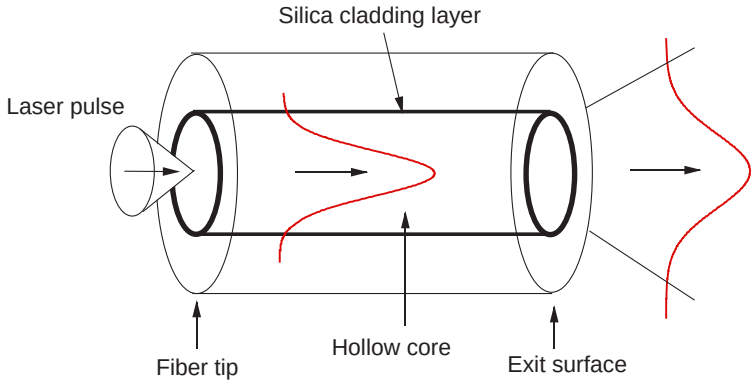

Figure 2: Schematic illustration of laser pulse propagation through kagome-lattice HC-PCF.

2.2 Initiation and Propagation of Fiber Fuse

On the other hand, fiber breakdown (fiber fuse) occurred at much lower energies (3.3 mJ and 7.6 mJ) than W_B (= 12 mJ) when employing a pulse duration of 12 ns [46]. This type of damage was very destructive. Once the fiber failed at the weak point, the damage propagated at a rate of about 0.05 m/s, also vaporizing, on its way, the kagome-lattice internal structure of the fiber.

Dumitrache *et al.* identified several mechanisms that may be responsible for this type of damage: laser power fluctuations and beam wandering, optical feedback caused by back-reflected light downstream of the fiber, and imperfections/microfractures inside the fiber [46]. Among them, optical feedback caused by back-reflected light will be fairly inhibited in the kagome-lattice HC-PCF.

They used a seven-cell hypocycloid-core and three-ring kagome lattice cladding HC-PCF in their pulse delivery experiments. The air-filling fraction of the

cladding structure was about 83% [54]. As can be seen from Fig. 1, the occupancy of silica (about 15%) in the cross section of the core and cladding layers is small and the index of refraction n inside the support tube of the fiber is estimated to be about 1.0675, which is close to that ($\sim$1) of air at room temperature. By using n, we obtain the coefficient of reflection R at the exit surface (see Fig. 2) of the fiber as

$$R = \left(\frac{n-1}{n+1}\right)^2. \tag{2}$$

The R at the exit surface was estimated to be only about 0.001. This means that the quantity of back-reflected light along the longitudinal direction of the kagome-lattice HC-PCF is very small. Therefore, optical feedback caused by back-reflected light downstream of the fiber, which is one of the damage mechanisms proposed by Dumitrache *et al.*, is considerably difficult to be realized in the kagome-lattice HC-PCF.

2.3 Physical Imperfections on Silica Strut Surface

It is a commonly observed phenomenon that surfaces tend to have a lower threshold for damage than the bulk material [55]–[59]. The ideas concerning the importance of the electric field strength at the surface of a dielectric material had been extended by Bloembergen to investigate the role of submicroscopic cracks, pores, and absorbing inclusions in the generation of surface damage [60], [61].

Physical imperfections on the surface of the silica strut is another of the damage mechanisms proposed by Dumitrache *et al.* First, we assume that there is a crack on the surface of the silica strut. If the crack is mathematically represented by a disk-shaped ellipsoidal void, with the lines of force in the silica strut normal to the disk, the electric field will be concentrated near the edge of the crack by a factor of n_s^2, where n_s (= 1.45) is the refractive index of the silica [61]. That is, the laser pulse intensity I_c near the edge of the crack is given by

$$I_c = n_s^4 I_s, \tag{3}$$

where I_s is the laser pulse intensity near the silica strut of the kagome-lattice cladding. I_s can be calculated by using

$$I_s = \eta \frac{1}{\pi}\left(\frac{W}{r_c^2 \tau_p}\right), \tag{4}$$

where W is the laser pulse energy and η is the theoretical optical power overlap ratio between the core and the cladding. Because the extinction ratio between the light intensity in the hollow (air) core and the kagome-lattice (silica) cladding is more than 40 dB [43], η becomes less than $\sim$0.01%.

As shown in Eq. (3), the intensity of the light pulse near the edge of the crack on the surface is higher by a light intensity enhancement factor (LIEF) of n_s^4

(= 5.06) than that near the silica strut. Furthermore, Génin *et al.* numerically calculated LIEF values for conical surface cracks [62]. They found that the LIEF values can locally reach two orders of magnitude higher than those for conical cracks of ideal shape and that theoretical LIEF values for the conical cracks range from 5 to 102 [62]. If we assume the maximum LIEF value (= 102), I_c becomes 1.4 $\times 10^8$ W/cm^2 using Eqs. (3) and (4), W = 3.3 mJ, τ_p = 12 ns, and η = 0.01%. This I_c value is three orders of magnitude smaller than the damage threshold intensity of silica [63]. This means that imperfections/microfractures inside the fiber, which is again a damage mechanism proposed by Dumitrache *et al.*, is not responsible for fiber fuse initiation in the kagome-lattice HC-PCF.

2.4 Absorbing Inclusions in Silica Strut

Next, we assume that there are absorbing inclusions in the surface of the silica strut. Commercial vitreous silica and soda-lime-silicate glasses contain metallic impurities such as iron and/or copper [64], [65]. The inclusion damage is associated with the presence of metallic absorbing particles in the silica glass. When spherical metallic particles are considered, they are generally considered to be opaque at the laser frequency and absorb energy from the laser beam. If the laser pulse of the beam is taken to be a square wave of a given duration, the average temperature $\hat{T}$ of the particle is expressed, neglecting any changes in phase, as [66]

$$\hat{T} = \left(\frac{3\epsilon_\lambda I_s}{4\rho C_v R_i} \right) \cdot t, \tag{5}$$

where ϵ_λ (= 0.3) is the spectral emissivity, and ρ, C_v, and R_i are the density, specific heat, and radius of the particle, respectively.

In the case of Fe inclusions with the pulse energy W of 3.3 mJ and $t = \tau_p$ (= 12 ns), $\hat{T}$ becomes

$$\hat{T} \approx 5.436 \times 10^{-5}/R_i, \tag{6}$$

where we used ρ = 7,870 kg m^{-3} and C_v = 442 J kg^{-1} K^{-1} [67]. As the thickness t_c of the silica strut is 0.28 μm, R_i must be smaller than t_c. If we assume R_i = 0.01 μm, $\hat{T}$ becomes 5,436 K for a certain range of particle sizes. As the silica glass is heated from room temperature, it melts in the vicinity of 1,996 K, turns into a liquid, and thermally decomposes near 3,000 K into a gas (SiO gas + O_2 gas) [68].

The estimated $\hat{T}$ (=5,436 K) is higher than the decomposition temperature (about 3,000 K) of the silica. Heat generated at the Fe particles is transmitted to the adjacent part of the silica strut, and the strut is heated. When the temperature of part of the silica strut rises to 3,000 K or higher, the optical absorption coefficient becomes on the order of 10^4 m^{-1}. As a result, heat generation due to light absorption also occurs in the strut. In this manner, the inclusion of metallic impurities in the silica struts is responsible for fiber fuse

initiation, and the fiber fails at the weak point, that is, where the kagome-lattice internal structure had been destroyed by the vaporization of the silica struts.

As the metal migration velocity in the silica glass is very low (47 μm/s [69]), the damage propagation velocity (about 0.05 m/s) will be attributable to the thermal wave propagation along the longitudinal direction of the fiber. In the following subsection, we describe the unsteady-state thermal conduction process in kagome-lattice HC-PCFs theoretically by the explicit finite-difference method on the basis of the thermochemical SiO_x production model.

3 Fiber Fuse Calculation of Kagome-Lattice HC-PCF

We used the simplified model shown in Fig. 3 for heat conduction analysis of the kagome-lattice HC-PCF. The hollow core was assumed to be a cylindrical rod of diameter $2r_c$ surrounded by a suitably designed cladding of high (silica ring) and low (air hole) refractive indices. The hollow core and air hole layer were assumed to be filled with air at the same temperature as the surrounding air (T_a).

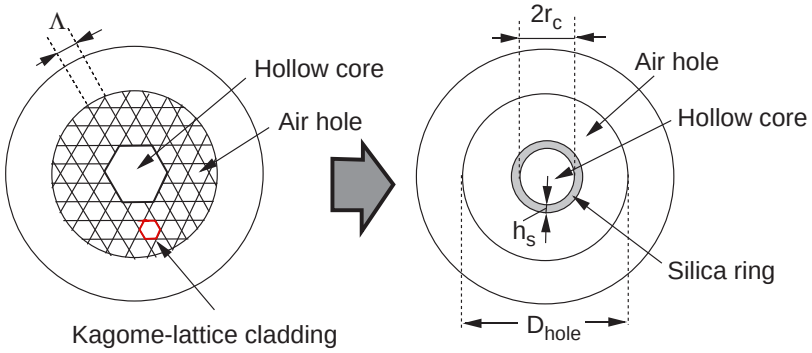

Figure 3: Heat conduction model for kagome-lattice HC-PCF.

In an actual kagome-lattice HC-PCF, many struts of silica glass exist in the kagome-lattice cladding, and the air-filling fraction η_s of the cladding structure is about 83%. If the width h_s of the silica ring is set to 8 μm ($\sim D_{hole}/20$), η_s becomes about 92%. This η_s is slightly larger than that (83%) of an actual kagome-lattice HC-PCF.

We assumed that the kagome-lattice HC-PCF is in an atmosphere with temperature $T = T_a$ and part of the silica ring of length ΔL (= 40 μm) is heated to a temperature of $T_c^0 (> T_a)$ owing to light absorption of metallic impurities, as shown in Fig. 4. Thus, as light propagates along the positive direction (away from the light source) in this part, a considerable amount of heat is produced

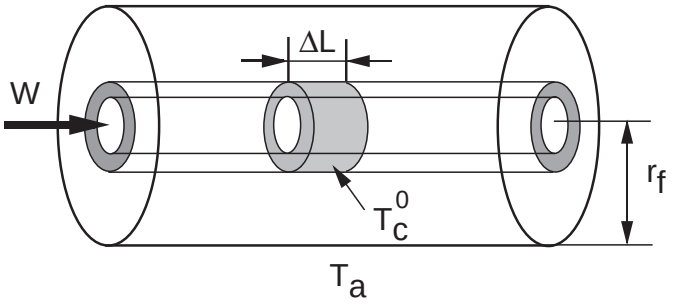

Figure 4: Hot zone in silica ring of kagome-lattice HC-PCF.

by light absorption. The calculation by the finite-difference method followed the procedure described in Part 2. However, in the case of a kagome-lattice HC-PCF, since the air layer exists outside the silica-ring layer, it is necessary to consider the boundary conditions, as described below.

When a certain quantity of heat per unit area (heat flux) is conducted from the heated silica-ring center to the end of the silica-ring layer ($r = r_c + h_s$) of an HC-PCF, a considerable amount of heat flux is transmitted through the air-hole layer with a temperature of T_a, and the residual heat flux stagnates in the core layer because the thermal conductivity λ of the air-hole layer is lower than that of silica glass (λ for air is about 1/300 that for glass). The stagnated heat flux in the silica-ring layer is used to heat air molecules existing in the hollow-core layer.

The heat transfer is a result of the air convection, which is generated by warming the air near the outer surface of the silica-ring layer. In this heat transfer, there is a region (called the "thermal boundary layer") near the outer surface of the silica-ring layer where the temperature of the air changes rapidly from a high value to T_a.

The boundary condition in this case is given by

$$\begin{aligned} -\lambda \left.\frac{\partial T}{\partial r}\right|_{r=r_c+h_s} &= \sigma_S \epsilon_e \left(T^4 - T_a^4\right) \\ &+ \frac{\lambda}{\delta r_t}\left(T - T_a\right), \end{aligned} \tag{7}$$

where σ_S is the Stefan–Boltzmann constant and ϵ_e ($\sim$0.9) is the emissivity of the surface. δr_t is the thickness of the thermal boundary layer and $\delta r_t = x\ \delta r$ is assumed in the HC-PCF calculation, where δr is the step size along the r axis and $x = 0.5$.

In the calculation, we set the time interval δt to 10 ns, the step size along the r axis δr to $r_f/20$, and the step size along the z axis δz to 20 μm, and assumed that $r_f = D_{hole}/2$, $T_c^0 = 3{,}000$ K, and $T_a = 298$ K. We used the following values of λ (W m^{-1} K^{-1}), ρ (kg m^{-3}), and C_p (J kg^{-1} K^{-1}) of air in the heat

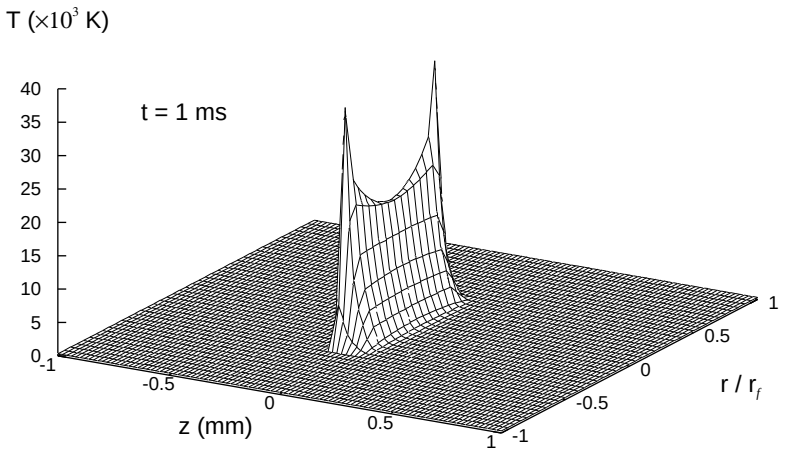

Figure 5: Temperature field in kagome-lattice HC-PCF after 1 ms when I = 1.61 MW/cm^2 at $\lambda_0 = 1.064$ μm.

conduction calculation [67].

$$\begin{aligned} \lambda &= 0.105 \\ \rho &= 0.183 \\ C_p &= 1,306 \end{aligned}$$

The laser light intensity I at the silica ring was increased to 1 MW/cm^2 and higher; then the thermal wave increased in size and propagated in the negative z direction toward the light source. We estimated the temperature field $T(r, z)$ of the kagome lattice HC-PCF at $t = 1$ ms and 6 ms after the incidence of laser light with $I = 1.61$ MW/cm^2 ($= 1.15$ I_s) and $\lambda_0 = 1.064$ μm. The calculated temperature fields are shown in Figs. 5 and 6. As shown in Fig. 5, the core center temperature near the end of the hot zone ($z \sim$ –0.06 mm) increases abruptly to about 1.9 $\times 10^4$ K after 1 ms. This rapid rise in the temperature initiates the fiber fuse propagation, as shown in Fig. 6. After 6 ms, the high-temperature front in the core reaches a z value of –0.58 mm. The average propagation velocity V_f was estimated to be 0.10 m/s using these data. This V_f is two times larger than that (0.05 m/s) observed by Dumitrache *et al.* [46] and it is about one-tenth that ($\sim$ 1 m/s) of the SMF28 optical fiber [70].

If there are absorbing inclusions such as Fe particles in the surface of the

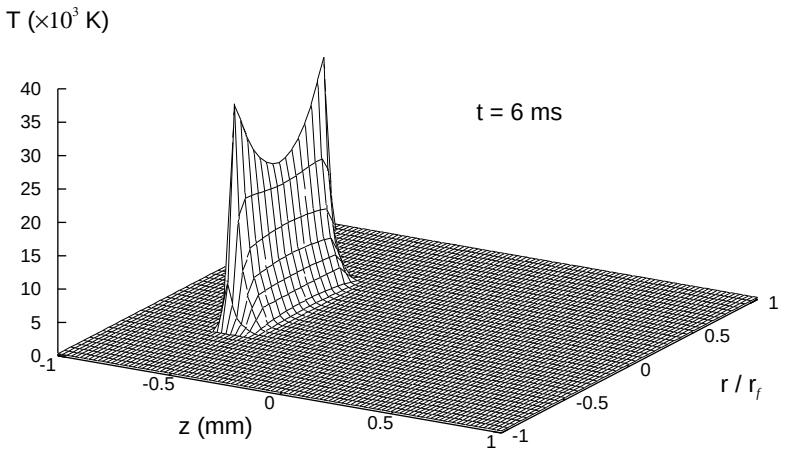

Figure 6: Temperature field in kagome-lattice HC-PCF after 6 ms when I = 1.61 MW/cm^2 at $\lambda_0 = 1.064$ μm.

silica ring, heat generated at the Fe particles is transmitted to the adjacent part of the silica ring, and the temperature of that part of the silica ring rises to 3,000 K. When I at the heated silica ring is increased to 1 MW/cm^2 and above, the thermal wave increases in size and propagates in the negative z direction toward the light source. In this way, the damage, starting at the heated part of the silica ring, propagates through the silica ring along the longitudinal direction of the fiber.

4 Revolver Fibers

The occurrence of a fiber fuse in a revolver fiber was first reported in 2018 by Kolyadin *et al.* [50]. They fabricated the two types of revolver fibers (RF1 and RF2) shown in Fig. 7. Both fibers have a relatively simple air–silica cladding structure, which consists of one layer of capillaries. In RF1, these capillaries touch each other, whereas they are located at a certain distance in RF2. In Fig. 7, the hollow core radius r_c, the inner diameter of the support tube D_{hole}, and the capillary thickness t_c of RF1/RF2 are 42/20 μm, 93/36 μm, and 3.1/0.8 μm, respectively. The support tube diameter ($2r_f$) of RF1/RF2 is 125/100 μm.

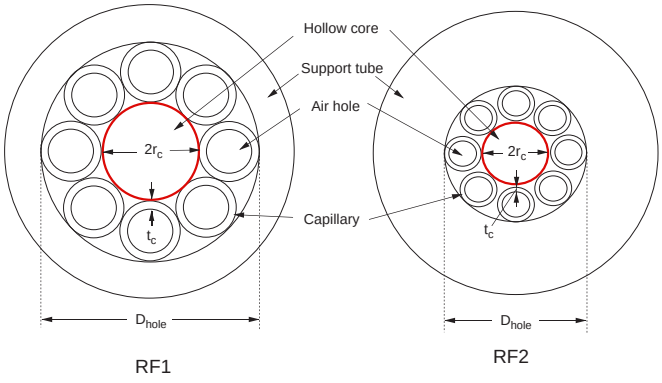

Figure 7: Two types of revolver fiber.

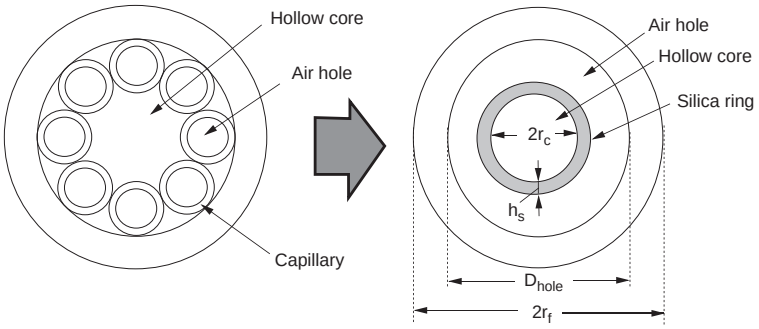

Figure 8: Heat conduction model for revolver fiber RF1.

4.1 Laser Source for Fiber Fuse Experiments

The fiber fuse experiments were carried out using a pulse laser operated at a wavelength (λ_0) of 1.064 μm. The laser radiation consisted of nanosecond trains of picosecond pulses (NTPPs) and had the duration of 130 ns. The fiber fuse initiation was observed in RF1 and RF2 at the average powers of about 4 W (RF1) and about 2 W (RF2), and the fiber fuse propagated at a velocity of about 1 m/s. The threshold power corresponded to the average intensity of 2.4 $\times 10^9$ W/cm^2 (RF1) and 5.2 $\times 10^9$ W/cm^2 (RF2) over the duration of the NTPP. These values were one order of magnitude smaller than the breakdown threshold intensity I_B (8.2 $\times 10^{10}$ W/cm^2 [53]) for air, which was estimated for the 10 ns pulsed laser operated at $\lambda_0 = 1.064$ μm.

For a revolver fiber, it is known that the extinction ratio of the power in the center of the hollow core to that in the silica capillary is more than 20 dB [16]. This means that the theoretical optical power overlap ratio between the

core and the cladding, η, becomes less than 1%. If η of 0.5% is assumed for the revolver fiber, the intensities I_s near the silica capillaries in RF1 and RF2 can be estimated to be 12 MW/cm^2 (RF1) and 26 MW/cm^2 (RF2) over the duration of the NTPP. These values are of the same magnitude as the I_{th} value (about 1–10 MW/cm^2) observed in the fiber fuse experiments using a CW laser operated at $\lambda_0 = 1.064$ μm [70].

4.2 Light Absorption by Metal Absorbent

In the experiments, a planar absorbing metal (absorbent) surface was brought parallel to the fiber end face [50]. In what follows, we used copper as the absorbing metal. When the laser beam was focused on the absorbent, the temperature of the laser-illuminated spot on the absorbent rose. The optical absorption coefficient α is related to the extinction coefficient k and λ_0 by [71]

$$\alpha = 4\pi k/\lambda_0. \tag{8}$$

A value of $k = 6.22$ for copper at $\lambda_0 = 0.95$ μm has been reported [72]. Using Eq. (8) and this k value, we estimated the absorption coefficient of copper to be $\alpha = 7.35 \times 10^7$ m^{-1} at $\lambda_0 = 1.064$ μm. This value is about three orders of magnitude larger than the α values (10^4 m^{-1} order) required for fiber fuse generation. The part of the silica capillaries in contact with the heated absorbent is also heated by thermal conduction and radiation from the absorbent. Then, this part starts to absorb the laser beam because of its absorption enhancement due to the temperature rise. The heated part of the capillaries also heats the surrounding area, which also starts to absorb the laser beam. As this process is repeated, the heated spot will move backward (toward the light source), as observed by Kolyadin *et al.* [50].

In the following subsection, we describe the unsteady-state thermal conduction process in a revolver fiber theoretically by the explicit finite-difference method on the basis of the thermochemical SiO_x production model.

5 Fiber Fuse Calculation of Revolver Fiber

We used the simplified model shown in Fig. 8 for heat conduction analysis of the revolver fiber. This model is similar to the multi-layered model proposed by Wang and Ding [21]. However, our model simplified the structure of revolver fiber, cpmpared with their multi-layered model. The hollow core was assumed to be a cylindrical rod of diameter $2r_c$ and it was surrounded by a suitably designed cladding of high (silica ring) and low (air hole) refractive indices. The hollow core and air hole layer were assumed to be filled with air at the same temperature as the surrounding air (T_a).

5.1 Fiber Fuse Propagation in RF1

In an actual revolver fiber RF1, eight capillaries of silica glass exist in the air–silica cladding, and the air-filling fraction η_s of the cladding structure is about

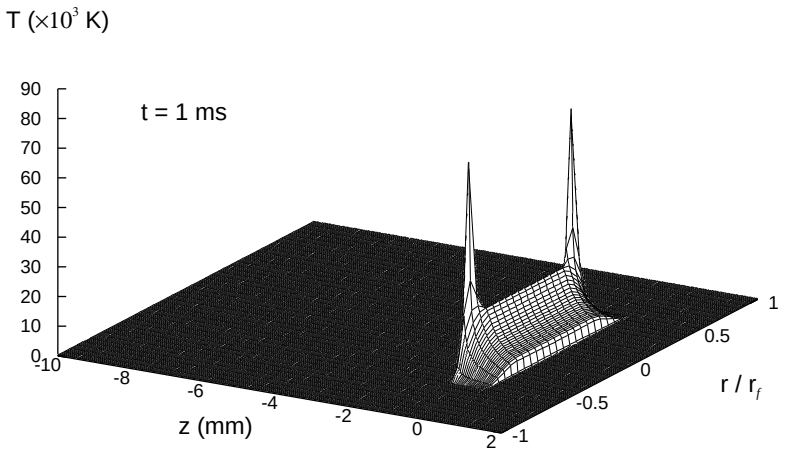

Figure 9: Temperature field in RF1 after 1 ms when $I = 18$ MW/cm^2 at $\lambda_0 = 1.064$ μm.

68%. If the width h_s of the silica ring is set to 11 μm ($\sim D_{hole}/8$), η_s becomes about 66%. This η_s is slightly smaller than that (68%) of an actual RF1.

Using the model described above, we investigated the appearance of the fiber fuse effect in a revolver fiber by the explicit finite-difference method. We assumed that the revolver fiber is in an atmosphere of temperature $T = T_a$ and part of the silica ring of length ΔL (= 40 μm) is heated to a temperature of $T_c^0 (> T_a)$, as shown in Fig. 4.

In the calculation, we set the time interval δt to 10 ns, the step size along the r axis δr to $r_f/20$, and the step size along the z axis δz to 20 μm and assumed that $T_c^0 = 3{,}000$ K and $T_a = 298$ K.

We estimated the temperature field $T(r, z)$ of the revolver fiber RF1 at $t =$ 1 ms and 8 ms after the incidence of laser light with $I = 18$ MW/cm^2 ($= 1.5 I_s$) and $\lambda_0 = 1.064$ μm. The calculated temperature fields are shown in Figs. 9 and 10. As shown in Fig. 9, the temperature of the silica-ring center near the end of the hot zone ($z =$ –0.96 mm) increases abruptly to about 7.1 $\times 10^4$ K after 1 ms. The heated part of the silica ring heats air molecules in the hollow core, in which the temperature also starts to increase. This rapid rise in the temperature initiates the fiber fuse propagation, as shown in Fig. 10. After 8 ms, the high-temperature front in the silica-ring center reaches a z value of –7.84 mm. The average propagation velocity V_f was estimated to be 0.98 m/s

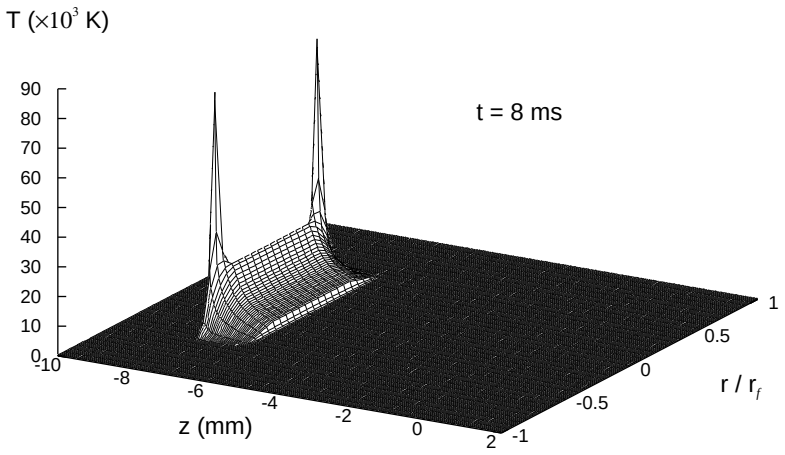

Figure 10: Temperature field in RF1 after 8 ms when $I = 18$ MW/cm^2 at $\lambda_0 = 1.064$ μm.

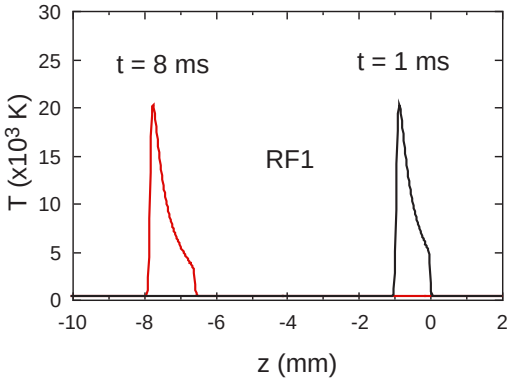

Figure 11: Temperature fields of the core center of RF1 after 1 ms and 8 ms when $I = 18$ MW/cm^2 and $\lambda_0 = 1.064$ μm.

using these data. This value is close to the V_f (1.0 m/s) observed by Kolyadin *et al.* [50] and is also the same value as that ($\sim$1 m/s) of the SMF28 optical fiber [70].

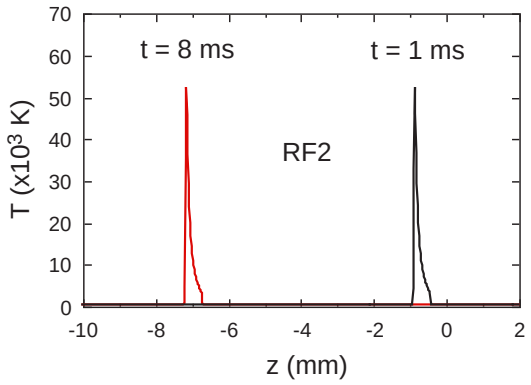

Figure 12: Temperature fields of the core center of RF2 after 1 ms and 8 ms when $I = 24$ MW/cm^2 and $\lambda_0 = 1.064$ μm.

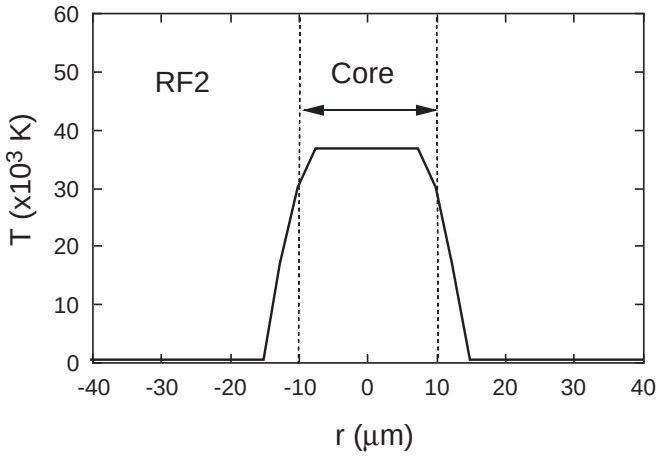

Figure 13: Temperature field near the high-temperature front of RF2 after 1 ms when $I = 24$ MW/cm^2 and $\lambda_0 = 1.064$ μm.

The temperature fields of the core center along the z direction were calculated at $t = 1$ ms and 8 ms after the incidence of laser light with $I = 18$ MW/cm^2 and $\lambda_0 = 1.064$ μm. The calculated results are shown in Fig. 11. The heat generated in the silica-ring layer is transferred to the neighboring core layers of the RF1. At a time of 1 ms after laser light incidence, a peak temperature (T_p) of 2.0 $\times 10^4$ K or above occurs in the center of the hollow-core layer. The T_p value is maintained after 8 ms, as shown in Fig. 11. The propagation velocity of the heated air is the same as that (0.98 m/s) of fiber fuse propagation.

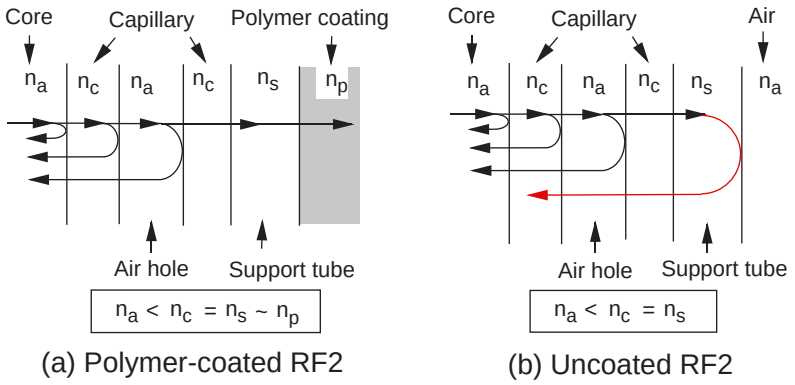

Figure 14: Schematic of light localization in core of polymer-coated RF2 (a) and uncoated RF2 (b).

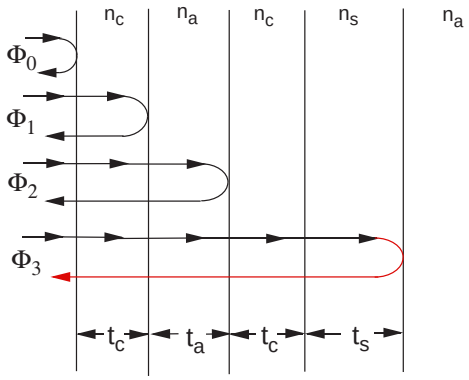

Figure 15: Optical routes in core of polymer-coated or uncoated RF2.

5.2 Fiber Fuse Propagation in Polymer-Coated RF2

Next, we investigated the unsteady-state thermal conduction process in the revolver fiber RF2 theoretically by the explicit finite-difference method, We used the simplified model shown in Fig. 8 for heat conduction analysis of the revolver fiber RF2. In an actual revolver fiber RF2, eight capillaries of silica glass exist in the air–silica cladding, and the air-filling fraction η_s of the cladding structure is about 79%. If the width h_s of the silica ring is set to 5 μm ($\sim D_{hole}/7$), η_s becomes about 44%. This η_s is smaller than that (79%) of an actual RF2. We assumed that the revolver fiber RF2 is in an atmosphere of temperature $T = T_a$, and part of the silica ring of length ΔL (= 40 μm) is heated to a temperature of $T_c^0 (> T_a)$, as shown in Fig. 4.

In the calculation, we set the time interval δt to 5 ns, the step size along the

r axis δr to $r_f/20$, and the step size along the z axis δz to 20 μm, and assumed that T_c^0 = 3,000 K and T_a = 298 K.

We estimated the temperature fields of the core center of the revolver fiber RF2 along the z direction at t = 1 ms and 8 ms after the incidence of laser light with I = 24 MW/cm^2 (= $0.93I_s$) and λ_0 = 1.064 μm. The calculated results are shown in Fig. 12.

As shown in Fig. 12, the core center temperature near the end of the hot zone (z = –0.86 mm) increases abruptly to about 5.2 $\times 10^4$ K after 1 ms. This rapid rise in the temperature initiates the fiber fuse propagation. After 8 ms, the high-temperature front in the core center reaches a z value of –7.14 mm. The average propagation velocity V_f was estimated to be 0.90 m/s using these data. This value is close to the V_f (0.91 m/s) observed by Kolyadin *et al.* [50]. In RF2, the T_p value (5.2 $\times 10^4$ K) is maintained after 8 ms, as shown in Fig. 12.

The temperature field near the high-temperature front after the incidence of laser light with I = 24 MW/cm^2 was calculated along the r direction at t = 1 ms. The calculated result is shown in Fig. 13.

As shown in the figure, the temperatures in the hollow core are higher than 3 $\times 10^4$ K, and the temperatures in the silica-ring layer decrease with increasing r and reach $\sim T_a$ at the end of the silica-ring layer. The temperature distribution shown in Fig. 13 is similar to the intensity distribution of optical-discharge plasma radiation in RF2 (Fig. 5(b) in [50]) observed by Kolyadin *et al.*

5.3 Fiber Fuse Propagation in Uncoated RF2

If RF2 was completely covered with a polymer coating, the measured V_f was 0.91 m/s [50]. However, if the polymer coating was partially removed and the silica support tube directly bordered air, the measured V_f became 2.84 m/s, which was three times larger than that of the polymer-coated RF2 [51].

RF2 consists of a hollow core and an air–silica cladding, which contains one layer of silica capillaries (see Fig. 7). In this fiber, the transverse components of a light wave along the radial direction propagate from the core to the silica capillary, and are then sent back to the core after being reflected at the core–capillary boundary and the inner and outer surfaces of the silica capillaries, as shown in Fig. 14 (a),

If the polymer coating of the RF2 is removed, the Fresnel reflection at the outer surface of the support tube occurs and the back-reflected light wave is incident upon the silica capillaries and the hollow core, as shown in Fig. 14 (b).

If all or several of the reflected waves stated above are in phase at the core–capillary boundary, then they are mutually enhanced as a consequence of constructive interference. To clarify the in-phase condition, we estimated four phase changes Φ_0–Φ_3 of optical routes shown in Fig. 15. Among them, Φ_3 is solely related to the uncoated RF2.

The phase change is accumulated by the radial translation and an additional phase change Φ_R due to the reflection [73]. Φ_R depends on the relative magnitude in the refractive indices of layers situated at both sides of the interface.

Table 1: Sellmeier parameters of pure silica [76].

Parameters	Pure SiO_2
c_1	0.6965325
c_2	0.4083099
c_3	0.8968766
b_1	0.004368309
b_2	0.01394999
b_3	97.93399

If a light wave travels from a low-index material to a high-index material, Φ_R becomes 0. Therefore, Φ_0 in Fig. 15 leads to 0. On the contrary, Φ_R becomes π when a light wave travels from a high-index material to a low-index material.

To determine the phase change due to radial translation, we need the lateral propagation constants denoted by

$$\kappa_i = \frac{2\pi}{\lambda_0}\sqrt{n_i^2 - n_{eff}^2} \quad (i = a, c, s), \tag{9}$$

where n_{eff} is the effective index of the least lossy mode of RF2 and λ_0 (= 1.064 μm) is the wavelength of the light wave. As n_{eff} of the fundamental mode is close to n_a (= 1.0) [74], [75] at $\lambda_0 = 1.064$ μm, Eq. (9) becomes

$$\kappa_i \approx \frac{2\pi}{\lambda_0}\sqrt{n_i^2 - 1} \quad (i = a, c, s). \tag{10}$$

The refractive index n of pure silica can be calculated using the Sellmeier equation:

$$n^2 - 1 = \sum_{i=1}^{3} c_i \lambda_0^2/(\lambda_0^2 - b_i), \tag{11}$$

where c_i and b_i are the parameters listed in Table 1 [76].

The n value of pure silica at $\lambda_0 = 1.064$ μm was calculated to be 1.44988 using Eq. (11). Therefore, in the calculation, we used $n_c = n_s = 1.452$ for the silica capillary and silica support tube at $\lambda_0 = 1.064$ μm. We also used $n_a = 1.0$, $t_c = 0.8$ μm, $t_a = 6.4$ μm, and $t_s = 32.0$ μm.

Let us consider the phase change Φ_1–Φ_3 shown in Fig. 15. To satisfy the in-phase condition responsible for Φ_0, waves reflected from the outer and inner surfaces of the silica capillary and the inner surface of the support tube must satisfy the following relations (Bragg conditions):

$$\Phi_1 - \Phi_0 = 2\kappa_c t_c + \pi = 2\pi m_1, \tag{12}$$

$$\Phi_2 - \Phi_0 = 2(\kappa_c t_c + \kappa_a t_a) = 2\pi m_2, \tag{13}$$

$$\Phi_3 - \Phi_0 = 2(\kappa_c t_c + \kappa_a t_a + \kappa_c t_c + \kappa_s t_s) + \pi = 2\pi m_3, \tag{14}$$

where m_1, m_2, and m_3 are integers. By substituting Eq. (10) into Eqs. (12)–(14), the following equations are derived:

$$nt_1 \equiv 4\sqrt{n_c^2 - 1}\, t_c = (2m_1 - 1)\lambda_0, \tag{15}$$

$$nt_2 \equiv 2\sqrt{n_c^2 - 1}\, t_c = m_2\lambda_0, \tag{16}$$

$$nt_3 \equiv 4(2\sqrt{n_c^2 - 1}\, t_c + \sqrt{n_s^2 - 1}\, t_s) = (2m_3 - 1)\lambda_0. \tag{17}$$

We calculated nt_1–nt_3 and estimated m_1–m_3 using Eqs. (15)–(17). The calculated results are shown in Table 2.

Table 2: Calculated parameters of phase conditions.

Parameter	Unit	Value
nt_1	μm	3.369
nt_2	μm	1.684
nt_3	μm	141.491
m_1	–	2.08
m_2	–	1.58
m_3	–	66.99

As shown in this table, m_2 (= 1.58) is not an integer, but m_1 (= 2.08) and m_3 (= 66.99) can be regarded as the integers 2 and 67. This means that the reflected waves from the outer surfaces of the silica capillary and support tube are in phase at the core–capillary boundary, and they are mutually enhanced as a consequence of the constructive interference.

As a result, the power in the hollow core and the silica capillary will be improved for the uncoated RF2 compared with the polymer-coated RF2. If the gain in power of 5 dB is assumed for the uncoated RF2, the intensity I_s near the silica capillaries in the uncoated RF2 can be estimated to be 76 MW/cm^2 over the duration of the NTPP.

We estimated the temperature fields of the core center of the uncoated RF2 along the z direction at $t = 1$ ms and 4 ms after the incidence of laser light with $I = 76$ MW/cm^2 and $\lambda_0 = 1.064$ μm. The calculated results are shown in Fig. 16.

As shown in Fig. 16, the core center temperature near the end of the hot zone (z = –2.06 mm) increases abruptly to about 5.5 $\times 10^4$ K after 1 ms. This rapid rise in the temperature initiates the fiber fuse propagation. After 4 ms, the high-temperature front in the core center reaches a z value of –8.38 mm. The average propagation velocity V_f was estimated to be 2.11 m/s using these data. This value is close to the V_f (2.84 m/s) observed by Bufetov *et al.* [51]. In the uncoated RF2, the T_p value (5.5 $\times 10^4$ K) is maintained after 4 ms, as shown in Fig. 16.

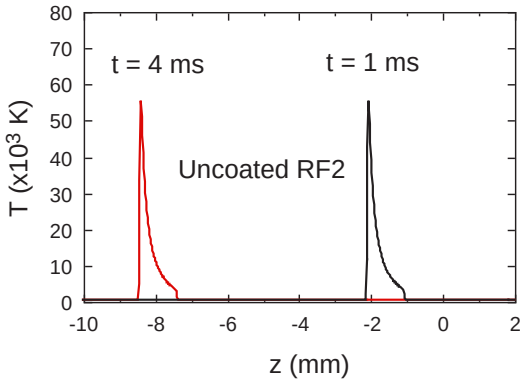

Figure 16: Temperature fields of the core center of uncoated RF2 after 1 ms and 4 ms when $I = 76$ MW/cm^2 and $\lambda_0 = 1.064$ μm.

5.4 Cavity Formation in RF2

When a fiber fuse was generated in RF2, the damage was in the form of periodic (or nonperiodic) cavities remaining in the fiber, and the periodic cavity interval Λ of the damage was about 170 μm [50] or 180 μm [51]. The periodicity of the cavities was sometimes significantly disturbed [51]. This Λ is about one order larger than that (13–22 μm) [77], [78] observed in conventional single-mode optical fibers with a CW laser source.

When CW laser light is incident upon an SMF, heat is generated continuously at the hot zone in the core layer owing to light absorption and the temperature of this part rises to 1×10^4 K and above. Then the thermal wave increases in size and starts to propagate in the negative z direction toward the light source. In this process, the periodic cavities with (relatively) small Λ values are formed in the SMF.

The relationship between the heat penetration time t_p and temperature penetration thickness δ in a silica glass layer is given by (see Appendix A)

$$\delta \simeq 3.6\sqrt{kt_p}, \tag{18}$$

where k is the thermal diffusivity. k values of silica glass at 500 K and 3,000 K are 4.40 $\times 10^{-6}$ m^2/s and 8.32 $\times 10^{-8}$ m^2/s, respectively. The relationship between t_p and δ in a silica glass layer was investigated at 500 K and 3,000 K. The calculated results are shown in Fig. 17.

As shown in Fig. 17, t_p values increase with increasing δ and the t_p values at 3,000 K are larger than those at 500 K. The t_p value at $\delta = 60$ μm is about 3,3 ms at 3,000 K.

In the fiber fuse experiments of RF2, a Nd:YAG laser with a repetition rate of 1,200 Hz was used as the pulse laser source. This means that the period of the NTPP is about 0.83 ms. This period is slightly shorter than the heat diffusion time (3.3 ms) through a 60-μm-thick glass layer at 3,000 K (see Fig. 17).

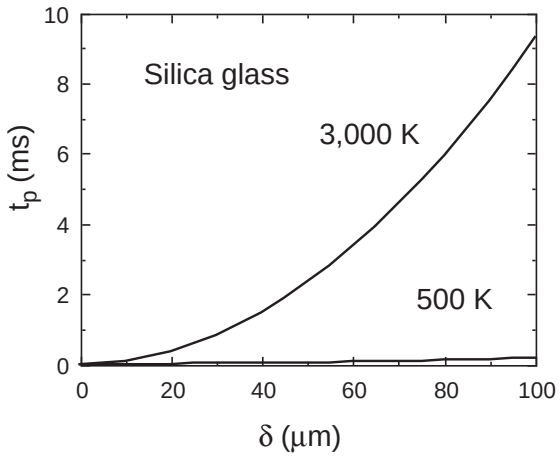

Figure 17: Relationship between t_p and δ in a silica glass layer.

On the other hand, it is well known that the first cavity length of fiber fuse propagation is a large value of 160–180 μm [78]. The duration of NTPPs is 130 ns [50], [51]. This duration is about one-tenth the time (18–30 μs) [78] for the formation of a second (short) cavity from the first long cavity during fiber fuse propagation.

When an NTPP is incident upon the RF2, heat generated at the silica capillary owing to light absorption is transmitted to the adjacent part of the capillary, and the temperature of that part rises to 3,000 K. Then the thermal wave increases in size and starts to propagate in the negative z direction toward the light source. In this way, the first long cavity is formed in the RF2. Then the heat in the capillaries is efficiently transferred in the air of the adjacent core and the long cavity is frozen after a quick shutdown of the laser source until the next NTPP arrives at RF2 after 0.83 ms. In this way, the formation of a long cavity with a large Λ (about 170 μm or 180 μm) is allowed to continue for each incidence of the NTPP upon RF2.

Bufetov *et al.* [51] explained the generation of a large Λ during fiber fuse propagation by adopting the concept of a laser-supported detonation wave (LSDW) and an attenuating shock wave (SW) as follows. Under the action of a picosecond (ps) laser pulse with the maximum intensity of 7.0 $\times 10^{11}$ W/cm^2, gas plasma is produced in the air by bringing the output end of RF2 into contact with a metal target; then an LSDW starts to propagate along the fiber towards the light source. The LSDW continues its movement as an attenuating SW after the end of the ps pulse. The maximum intensity (7.0 $\times 10^{11}$ W/cm^2) of the ps pulse is one order of magnitude larger than the breakdown threshold intensity (8.2 $\times 10^{10}$ W/cm^2 [53]) for air. Therefore, the point explosion due to the optical breakdown of air will occur around major peaks of ps pulses. The

motion of the gas plasma after the cessation of the laser pulse can be estimated on the basis of the point explosion theory with spherical symmetry [79], [80]. According to this theory, the gas plasma in the SW expands as

$$L(t) = \left(\frac{W}{\rho_0}\right)^{1/5} \cdot t^{2/5}, \tag{19}$$

where L is the distance from the center of the explosion, W (= 0.17 mJ) is the energy of the ps pulse, and ρ_0 (= 1.3 kg/m^3) is the initial density of air in the core of RF2. As the period of the ps pulses is 13 ns, L at t = 13 ns is estimated to be about 117 μm using Eq. (19). This L value is close to the Λ value (about 170 μm or 180 μm) observed in RF2.

When the next ps pulse arrives 13 ns later, the expanded gas plasma of the SW is not completely relaxed in the hollow core. Hence, the next pulse is absorbed in the front of a still-powerful SW. As a result, the propagation of the LSDW and its relaxation are repeated, forming several cavities with large Λ along the fiber towards the light source. The evolution number N_{pe} of the point explosion during the period (0.83 ms) of the NTPP is highly affectd by laser power fluctuation. The changes in N_{pe} result in a disturbance of the periodicity of the cavities, as observed by Bufetov *et al.* [51].

6 Hollow Optical Fiber

The fiber fuse effect in hollow optical fibers (HOFs) was investigated by Ha *et al.* [81]. In contrast to PCFs, the HOF guides the light by the index difference between the ring core and other boundaries in the central air hole and the silica cladding. Ha *et al.* fabricated HOFs with a three-layer structure, as shown in Fig. 18. The central air hole of diameter D_{hole} was surrounded by a high-index ring core and silica cladding. The thickness d_c and the refractive index difference between the core and cladding Δ of the ring core layer were 2.6 μm and 0.45% [82], respectively, and D_{hole} of 4 μm or 6 μm was used in the fiber fuse experiments. The HOF diameter was 125 μm. In the following, the HOFs with D_{hole} = 4 μm and 6 μm are referred to as HOF4 and HOF6, respectively.

The fiber fuse experiments were carried out using a high-power CW laser operated at λ_0 = 1.064 μm. Fiber fuse propagation was observed in HOF4 upon exposure to CW laser light with P_0 = 4 W. On the other hand, fiber fuse initiation and propagation were not observed in HOF6 irradiated at P_0 of up to 6.35 W [81].

In the following, thermal conduction analysis for the case that a high power at λ_0 = 1.064 μm is incident on an HOF is performed and the results of simulating the fiber fuse behavior in the HOF are described.

6.1 Fiber Fuse Calculation of HOF

We used the simplified model shown in Fig. 18 for heat conduction analysis of the HOF. The air hole layer was assumed to be filled with air at $T = T_a$. Using

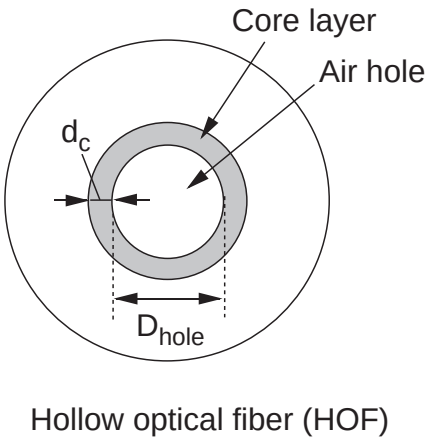

Figure 18: Schematic cross section of hollow optical fiber.

the model described above, the appearance of the fiber fuse effect in the HOF was investigated by the explicit finite-difference method.

We assumed that the HOF is in an atmosphere with temperature $T = T_a$ and part of the core layer of length ΔL (= 40 μm) is heated to a temperature of $T_c^0 (> T_a)$, as shown in Fig. 19.

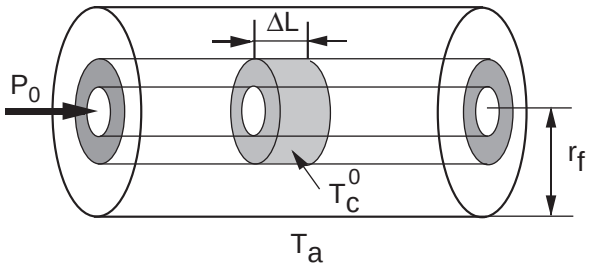

Figure 19: Hot zone in core layer of HOF.

Figure 20 shows the intensity profile of the fundamental core mode of the HOF. As shown in Fig. 20, it is clear that the intensity (or power) is widely distributed in the core and cladding layers and the power fraction at the central air hole is very small (about 0.035% at $\lambda_0 = 1.064$ μm [82]). The effective cross-sectional areas A_{eff} of HOF4 and HOF6 were reported to be 156.5 μm^2 and 164.6 μm^2, respectively [81]. The power fraction in the core layer was assumed to be about 0.0327 for HOF4 and about 0.0199 for HOF6 at $\lambda_0 = 1.064$ μm.

First, we investigated the temperature fields in HOF4 after the incidence of a laser power P_0 of up to 8 W in the experiments carried out by Ha *et al.* [81].

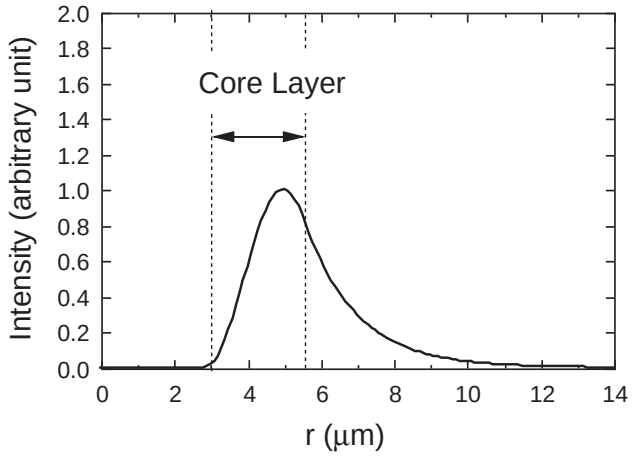

Figure 20: Intensity profile of HOF.

In the calculation, we set the time interval δt to 10 ns, the step size along the r axis δr to $r_f/20$, and the step size along the z axis δz to 20 μm, and assumed that $T_c^0 = 2{,}923$ K and $T_a = 298$ K.

We estimated the change in the temperature at the air-hole center ($r = 0$ μm) in HOF4 with time after the incidence of laser light with $P_0 = 3$ W and $\lambda_0 = 1.064$ μm. The calculated temperatures are shown in Fig. 21. As shown

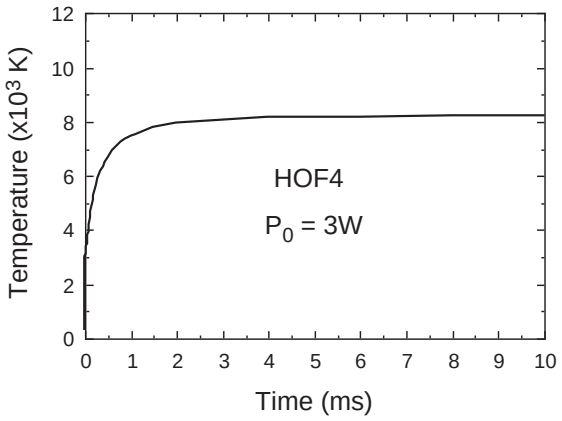

Figure 21: Temperature at the air-hole center in HOF4 vs time after the incidence of laser light with $P_0 = 3$ W and $\lambda_0 = 1.064$ μm.

in Fig. 21, the temperature at the end ($z = 0$ mm) of the hot zone rapidly increases to a large value of $\geq$ 8,000 K after 2 ms.

Then we estimated the temperature field $T(r, 0)$ of the stationary thermal wave at the end ($z = 0$ mm) of the hot zone in HOF4 at $t = 4$ ms after the incidence of laser light with $\lambda_0 = 1.064$ μm and an initial power P_0 of 0–8 W. The calculated temperature fields are shown in Fig. 22.

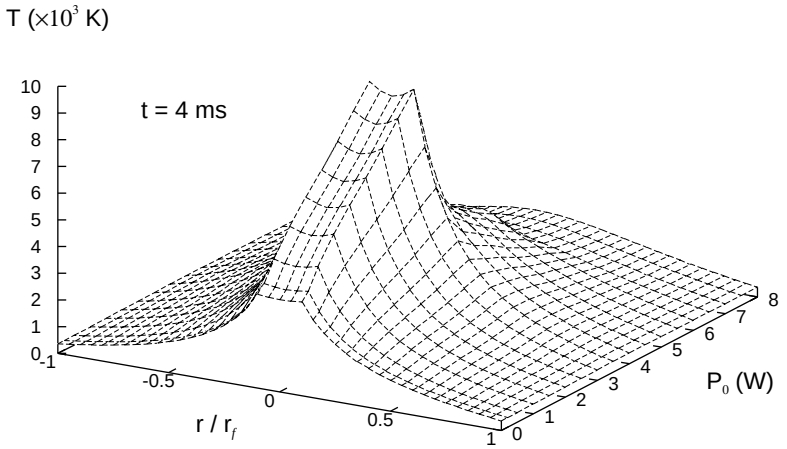

Figure 22: Temperature fields of the stationary thermal wave at the end of the hot zone in HOF4 after 4 ms when $P_0 = 0$–8 W and $\lambda_0 = 1.064$ μm.

When the power of the light entering HOF4 increases from 0 W to 1 W, a thermal wave with a temperature of higher than 5,000 K is generated at the end of the hot zone, as shown in Fig. 22. The central temperature of the stationary thermal wave increases with increasing P_0 and reaches about 8,900 K at $P_0 =$ 3.5 W. Then it decreases with increasing P_0 and reaches about 1,800 K at $P_0 =$ 8 W. This result agrees with the experimental result observed by Ha *et al.* [81].

If P_0 is further increased to 4 W and above, the thermal wave will increase in size and propagate in the negative z direction toward the light source. We estimated the temperature field $T(r, z)$ of HOF4 at $t = 4$ ms and 14 ms after the incidence of laser light with $P_0 = 4$ W and $\lambda_0 = 1.064$ μm. The calculated temperature fields are shown in Figs. 23 and 24. As shown in Fig. 23, the central temperature near the end of the hot zone ($z \sim$ –0.02 mm) changes abruptly to a high value of about 9,300 K after 4 ms. This rapid rise in the temperature initiates the fiber fuse propagation, as shown in Fig. 24. After 14 ms, the high-temperature front in the core layer reaches a z value of –0.12 mm. The average propagation velocity V_f was estimated to be 0.01 m/s using these

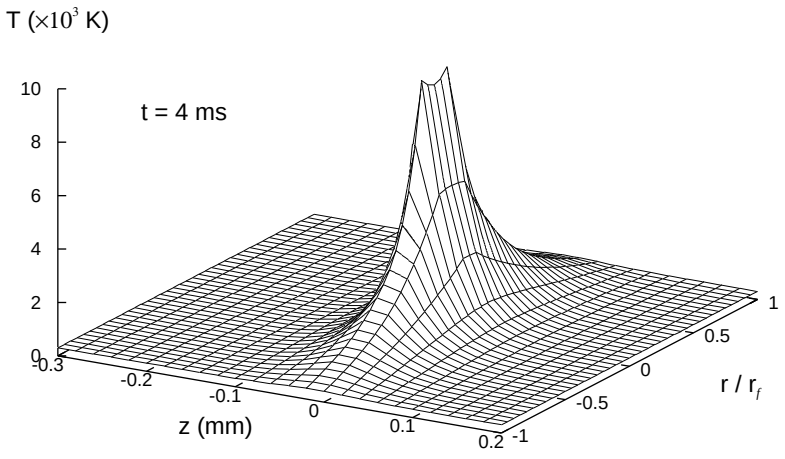

Figure 23: Temperature field in HOF4 after 4 ms when $P_0 = 4$ W at $\lambda_0 = 1.064$ μm.

data. This V_f is about one-hundredth the value ($\sim$1 m/s) of the SMF28 optical fiber [70] and is close to the velocity (about 0.02 m/s) of a polymer optical fiber [83] and that (about 0.05 m/s) of a hollow core kagome lattice fiber [46].

Next, we investigated the temperature fields in HOF6 after the incidence of a laser power P_0 of up to 10 W. We estimated the temperature fields $T(r, 0)$ of the stationary thermal wave at the end ($z = 0$ mm) of the hot zone in HOF6 at $t = 4$ ms after the incidence of laser light with $\lambda_0 = 1.064$ μm and an initial power P_0 of 0–10 W. The calculated temperature fields are shown in Fig. 25.

When the power of the light entering HOF6 increases from 0 W to 1.5 W, a thermal wave with a peak temperature of higher than 5,000 K is generated at the end of the hot zone, as shown in Fig. 25. The peak temperature of the stationary thermal wave increases with increasing P_0 and reaches about 9,000 K at $P_0 = 6$ W. Then it decreases with increasing P_0 and reaches about 3,000 K at $P_0 = 10$ W. This result agrees with the experimental result observed by Ha *et al.* [81].

6.2 Formation of Tadpole-Like Cavity in HOF

Ha *et al.* reported the formation of a unique tadpole-like cavity in HOF4 during fiber fuse propagation [81]. The formation of this cavity may be considered to

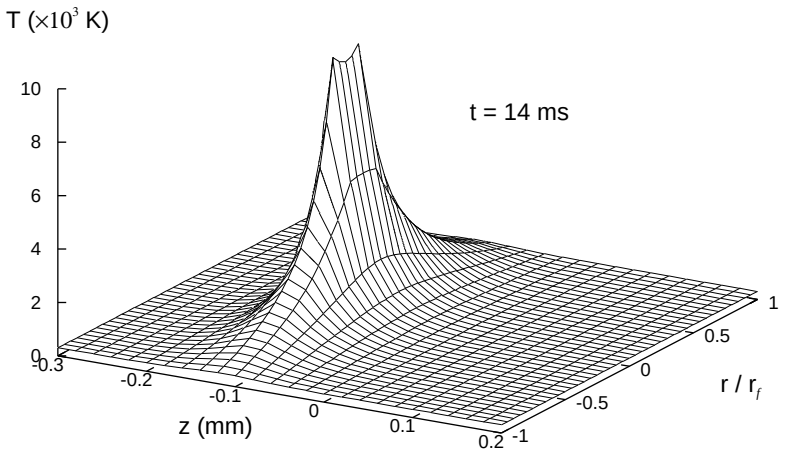

Figure 24: Temperature field in HOF4 after 14 ms when $P_0 = 4$ W at $\lambda_0 = 1.064$ μm.

occur as follows.

Silica glass has a melting temperature of $T_m = 1{,}996$ K. If solid silica glass is heated above T_m, it becomes a liquid "melt" and its viscosity decreases with increasing temperature. As shown in Figs. 23 and 24, the temperature in the vicinity of the high-temperature front exceeds T_m of the silica glass. The longitudinal length of the area whose temperature exceeds T_m is about 80 μm (see Figs. 23 and 24). Therefore, the silica glass in this area will behave as a liquid melt and the adjacent air hole layer will be filled with melted silica because of the small diameter (= 4 μm) of the air hole layer. When the melted silica protrudes into the air hole layer along the radial (r) direction for a short time, both temperature and viscosity distributions are formed along the longitudinal direction of the protruding silica, as shown in Fig. 26.

As the viscosity in the area neighboring the high-temperature front is very low, the melted silica in this area can freely expand and its density decreases. In contrast, at the end point of the area, the melted silica contracts and its density increases.

As described in 1.4.2, when silica glass is heated to high temperatures of above 3,000 K, molecular oxygen (O_2) is produced owing to the thermal decomposition of SiO_2. If there are both compressed and rarefied parts in the protruding silica, the O_2 gas diffuses from the compressed part into the rarefied

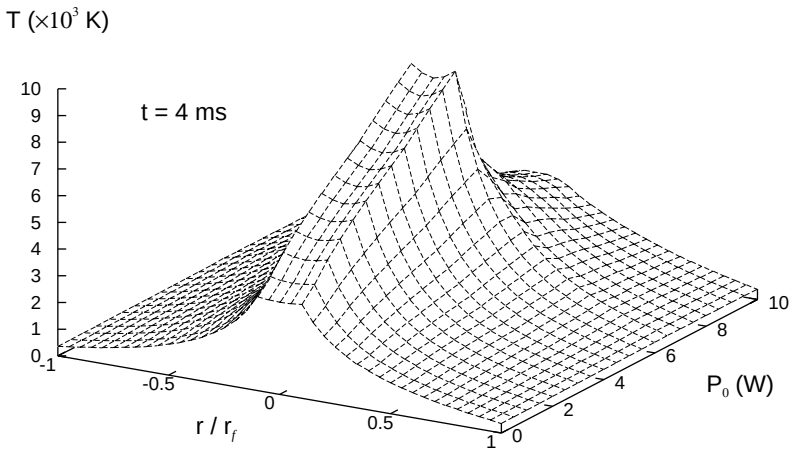

Figure 25: Temperature fields of the stationary thermal wave at the end of the hot zone in HOF6 after 4 ms when $P_0 = 0$–10 W and $\lambda_0 = 1.064$ μm.

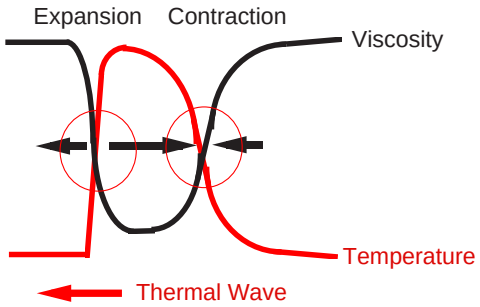

Figure 26: Schematic temperature and viscosity distributions in the protruding silica.

part in a short time. If a large amount of O_2 gas accumulates in the rarefied part of the silica, bubbles (cavities) are formed in this part. In this manner, unique tadpole-like cavities are formed in HOF4 during fiber fuse propagation. The interval Λ between the tadpole-like cavities was estimated to be 70 μm [81]. This length is close to the longitudinal length (about 80 μm) of the area whose temperature exceeds T_m.

The relationship between the period Φ of the oscillatory motion of the melted silica and the velocity V_f of fiber fuse propagation is given by (see 3.3.1)

$$\Lambda = \Phi V_f. \tag{20}$$

Φ was estimated to be 7 ms using Eq. (20) with $\Lambda = 70$ μm and V_f ~0.01 m/s. As shown in Fig. 17, the heat penetration time t_p increases with increasing temperature penetration thickness δ and the t_p value at $\delta = 60$ μm is about 3,3 ms at 3,000 K. Consequently, the Φ value of 7 ms is about twice the time (3.3 ms) required for the heat penetration through a 60-μm-thick silica glass layer at 3,000 K.

6.3 Estimation of Penetration Length in HOF

Ha *et al.* defined the length between the splice point and the termination point of a fiber fuse as the penetration length L_p. They reported that when the power P_0 of the light entering HOF6 increases from 1.5 W to 6 W, L_p increases from 60 μm to 840 μm [81]. The L_p values for HOF6 are listed in Table 3.

If the high-temperature thermal wave of a fiber fuse enters from an SMF into HOF6, heat is generated in the core layer of HOF6 adjacent to the splice point. A certain quantity of heat stagnating in the core layer is dissipated by heat transfer between the inner surface of the core layer and the air in the hole layer with a temperature of T_a (= 298 K). As a result, the temperature of the air hole layer increases. If T_{av} is defined as the average temperature of the inner surface of the core layer and the air hole layer, T_{av} is almost equal to the temperature of the air-hole center in HOF6, as shown in Fig. 27. T_{av} increases with increasing incident power P_0, as shown in Table 3. Moreover, T_p, the peak

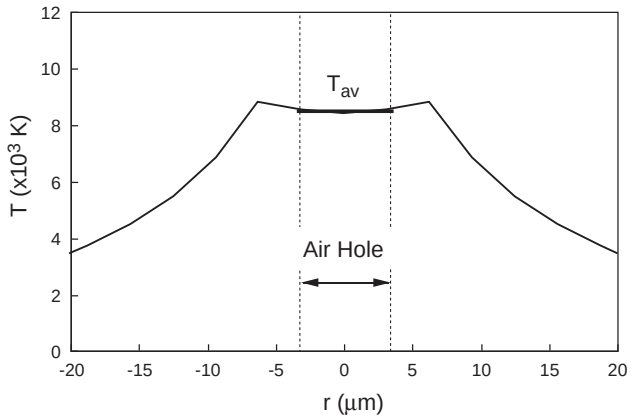

Figure 27: Average temperature of air hole layer.

temperature of the thermal wave propagating in the SMF, also increases with increasing P_0, as shown in Table 3.

Table 3: Parameters for HOF6.

P_0 (W)	L_p (μm)	T_{av} (K)	T_p (K)	V_f (m/s)
1.5	60	5,020	33,960	0.44
2	80	5,470	34,010	0.54
3	110	6,280	39,700	0.74
4	230	7,040	48,570	0.91
5	450	7,980	57,900	1.05
6	840	8,850	60,140	1.18

In Table 3, the T_p and V_f values for SMF28 were theoretically estimated by the finite-difference method. Details of this calculation are described in Chap. 2.

We define the time between the entry of the thermal wave into the air hole layer of HOF6 passing through the splice point and the collapse of an adjacent air hole layer with the melted silica as the time delay τ. The penetration length L_p^1 owing to this first process is expressed using V_f and τ as follows:

$$L_p^1 \approx \tau \cdot V_f. \tag{21}$$

When $P_0 = 1.5$ W, τ was estimated to be about 136 μs using Eq. (21) with L_p^1 = 60 μm and V_f ~0.44 m/s. This value (= 136 μs) is about six times larger than the time (about 20 μs) for the formation of one cavity for SMF28 [78] and it is close to t_p (134 μs) for the heat penetration through a 12-μm-thick silica glass layer at 3,000 K (see Fig. 17). As τ is considered to be invariant when P_0 increases from 1.5 W to 6 W, we estimated L_p^1 at P_0 of 1.5–6 W. The calculated results are shown in Table 4.

Table 4: Penetration lengths for HOF6.

P_0 (W)	L_p^1 (μm)	L_p^2 (μm)	$L_p^{(1+2)}$ (μm)	L_p (μm)
1.5	60	4.5	64.5	60
2	73	10.0	83.0	80
3	101	36.4	137.4	110
4	124	107.5	231.5	230
5	143	316.6	459.6	450
6	160	622.3	782.3	840

As shown in Table 4, the calculated L_p^1 values are smaller than the experimental L_p values except when $P_0 = 1.5$ W.

This discrepancy may be resolved by considering the slow fluid flow of the melted silica in the air hole layer. The following relationship is known to hold

between the temperature T and pressure p of a gas plasma [84]:

$$p = N_g k_B T, \tag{22}$$

where N_g is the number density of a Si + O atomic gas. We assumed N_g ~0.8 $\times 10^{22}$ cm^{-3}, which is the average number density of Si in the temperature range of 3,000–10,000 K (see 1.5.1 and [85]). p is proportional to T, as shown by Eq. (22). Therefore, it can be expected that p of the high-temperature thermal wave of the fiber fuse is larger than that of the air hole layer because the peak temperature (T_p) of the thermal wave is higher than the average temperature (T_{av}) of the air hole layer (see Table 3). This pressure gradient will become small after the first penetration process. We assumed that the pressure gradient after the first penetration process is less than that before this process by a factor of 0.1. This small pressure gradient results in the Hagen–Poiseuille flow [86] of the melted silica in the longitudinal direction of the air hole layer, as shown in Fig. 28.

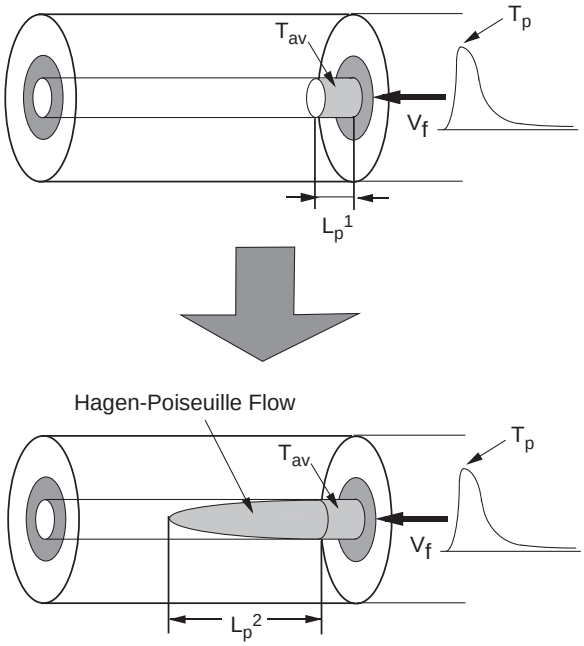

Figure 28: Penetration in the air hole layer.

By considering the steady motion of a fluid through a circular tube under the influence of a pressure gradient, the volumetric rate of flow (or flux) Q across the circular cross section of radius a (= 3 μm) is given by [87]

$$Q = -\frac{\pi a^4 f}{8\eta} \cdot \frac{\partial p}{\partial z}, \tag{23}$$

where η is the viscosity of the melted silica, $f = 10^{-1}$, and $-\partial p/\partial z$ is the pressure gradient between the pressure at the peak temperature (T_p) of the thermal wave and that at the average temperature (T_{av}) of the melted silica in the air hole layer. We assumed that the distance Δz between the peak position of the thermal wave and the end face of the penetrating part of the melted silica is equal to L_p^1. η (unit: P) of the melted silica is related to the temperature T (unit: K) by the following equation [88]:

$$\log \eta = -6.24 + 26,950/T. \tag{24}$$

Using Eq. (23), the penetration length L_p^2 owing to the Hagen–Poiseuille flow after 10 ms is given by

$$L_p^2 = 0.01 \frac{Q}{\pi a^2}. \tag{25}$$

We estimated the L_p^2 values at P_0 of 1.5–6 W using Eqs. (22)–(25). The calculated results are shown in Table 4. In this table, $L_p^{(1+2)}$ is the sum of L_p^1 and L_p^2. The calculated $L_p^{(1+2)}$ values are close to the experimental L_p values observed by Ha *et al.* [81].

A Temperature Penetration Thickness

The semi-infinite solid provides a useful idealization for many practical problems. It is used to approximate the transient response of a finite solid, such as a thin silica glass layer.

The unsteady heat conduction equation in a semi-infinite solid is given by

$$\frac{\partial T}{\partial t} = \kappa \frac{\partial^2 T}{\partial x^2}, \quad k = \frac{\lambda}{\rho C_p}, \tag{D1}$$

k is the thermal diffusivity and λ, ρ, and C_p are the thermal conductivity, density, and specific heat, respectively. To solve Eq. (D1) for the temperature distribution $T(x,t)$, it is necessary to specify an initial dondition and two interior boundary conditions. The initial condition is

$$T(x,0) = T_0 \tag{D2}$$

and the boundary conditions are

$$T(0,t) = T_s, \quad T(\infty,t) = T_0 \tag{D3}$$

The solution is obtained by introducing a similarity variable $\eta = x/2\sqrt{kt}$, through which the heat equation is transformed from a partial differential equation, involving two independent variables (x and t), to an ordinary differential equation expressed in terms of the single similarity variable [89].

Using η, Eq. (D1) becomes

$$\frac{\partial^2 T}{\partial \eta^2} + 2\eta \frac{\partial T}{\partial \eta} = 0. \tag{D4}$$

The general solution of Eq. (D4) is given by

$$T = C_1 \cdot erf(\eta) + C_2, \tag{D5}$$

where C_1 and C_2 are the undetermined constants and $erf(\eta)$ is the Gaussian error function, which is given by

$$erf(\eta) = \frac{2}{\sqrt{\pi}} \int_0^{\eta} \exp\left(-u^2\right) du. \tag{D6}$$

C_1 and C_2 are determined by applying the intial and boundary conditions as

$$C_1 = T_0 - T_s, \quad C_2 = T_s. \tag{D7}$$

By substituting Eq. (D7) into Eq. (D5), the following equation is derived

$$\frac{T - T_0}{T_s - T_0} = 1 - erf(\eta). \tag{D8}$$

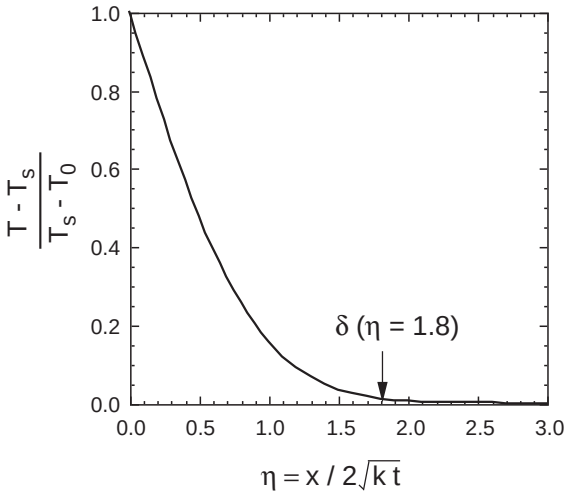

Figure 29: Temperature distribution in semi-infinite solid.

Temperature distribution in a semi-infinite solid was estimated using Eq. (D8). The calculated result is shown in Fig. 29. As shown in this figure, $(T-T_s)/(T_s-T_0)$ decreases with increasing η and gradually approaches zero at $\eta = 3$. The temperature penetration thickness δ and heat penetration time t_p are defined as the distance x and time t at which $(T-T_s)/(T_s-T_0) = 0.01$ and $\eta \simeq 1.8$ [90]. When $\eta \simeq 1.8$, the relationship between δ and t_p is given by

$$\delta \simeq 3.6\sqrt{kt_p}. \tag{D9}$$

References

[1] P. St. J. Russell, "Photonic crystal fibers," *Science*, Vol. 299, pp. 358–362, 2003.

[2] F. Couny, F. Benabid, P. J. Roberts, P. S. Light, and M. G. Raymer, "Generation and photonic guidance of multi-octave optical-frequency combs," *Science*, Vol. 318, pp. 1118–1121, 2007.

[3] F. Benabid, J. C. Knight, G. Antonopoulos, and P. Russell, "Stimulated Raman scattering in hydrogen-filled hollow-core photonic crystal fiber," *Science*, Vol. 298, pp. 399–402, 2002.

[4] Y. Y. Wang, X. Peng, M. Alharbi, C. Fourcade-Dutin, T. D. Bradley, F. Gérôme, M. Mielke, T. Booth, and F. Benabid, "Design and fabrication of hollow-core photonic crystal fibers for high-power ultrashort pulse transportation and pulse compression," *Opt. Lett.*, Vol. 37, No. 15, pp. 3111–3113, 2012.

[5] T. D. Bradley, Y. Wang, M. Alharbi, B. Debord, C. Fourcade-Dutin, B. Beaudou, F. Gerome, and F. Benabid, "Optical properties of low loss (70dB/km) hypocycloid-core kagome hollow core photonic crystal fiber for Rb and Cs based optical applications," *IEEE J. Lightwave Technol.*, Vol. 31, No. 16, pp. 2752–2755, 2013.

[6] N. V. Wheeler, T. D. Bradley, J. R. Hayes, M. A. Gouveia, S. Liang, Y. Chen, S. R. Sandoghchi, S. M. A. Mousavi, F. Poletti, M. N. Petrovich, and D. J. Richardson, "Low-loss kagome hollow-core fibers operating from the near- to the mid-IR," *Opt. Lett.*, Vol. 42, No. 13, pp. 2571–2574, 2017.

[7] M. Maurel, M. Chafer, A. Amsanpally, M. Adnan, F. Amrani, B. Debord, L. Vincetti, F. Gérôme, and F. Benabid, "Optimized inhibited-coupling kagome fibers at Yb-Nd:Yag (8.5 dB/km) and Ti:Sa (30 dB/km) ranges," *Opt. Lett.*, Vol. 43, No. 7, pp. 1598–1601, 2018.

[8] Y. Y. Wang, N. V. Wheeler, F. Couny, P. J. Roberts, and F. Benabid, "Low loss broadband transmission in hypocycloid-core kagome hollow-core photonic crystal fiber," *Opt. Lett.*, Vol. 36, No. 5, pp. 669–671, 2011.

[9] B. Debord, M. Alharbi, T. D. Bradley, C. Fourcade-Dutin, Y. Y. Wang, L. Vincetti, F. Gérôme, and F. Benabid, "Hypocycloid-shaped hollow-core photonic crystal fiber Part I: arc curvature effect on confinement loss," *Opt. Express*, Vol. 21, No. 23, pp. 28597–28608, 2013.

[10] A. D. Pryamikov, A. S. Biriukov, A. F. Kosolapov, V. G. Plotnichenko, S. L. Semjonov, and E. M. Dianov, "Demonstration of a waveguide regime for a silica hollow-core microstructured optical fiber with a negative curvature of the core boundary in the spectral region > 3.5 μm," *Opt. Express*, Vol. 19, No. 2, pp. 1441–1448, 2011.

[11] A. F. Kosolapov, A. D. Pryamikov, A. S. Biriukov, V. S. Shiryaev, M. S. Astapovich, G. E. Snopatin, V. G. Plotnichenko, M. F. Churbanov, and E. M. Dianov, "Demonstration of CO_2-laser power delivery through chalcogenide-glass fiber with negative-curvature hollow core," *Opt. Express*, Vol. 19, No. 25, pp. 25723–25728, 2011.

[12] F. Yu and J. C. Knight, "Spectral attenuation limits of silica hollow core negative curvature fiber," *Opt. Express*, Vol. 21, No. 18, pp. 21466–21471, 2013.

[13] A. N. Kolyadin, A. F. Kosolapov, A. D. Prymikov, A. S. Biriukov, V. G. Plotnichenko, and E. M. Dianov, "Light transmission in negative curvature hollow core fiber in extremely high material loss region," *Opt. Express*, Vol. 21, No. 8, pp. 9514–9519, 2013.

[14] W. Belardi and J. C. Knight, "Hollow antiresonant fibers with reduced attenuation," *Opt. Lett.*, Vol. 30, No. 7, pp. 1853–1856, 2014.

[15] W. Belardi and J. C. Knight, "Hollow antiresonant fibers with low bending loss," *Opt. Express*, Vol. 22, No. 8, pp. 10091–10096, 2014.

[16] F. Poletti, "Nested antiresonant nodeless hollow core fiber," *Opt. Express*, Vol. 22, No. 20, pp. 23807–23828, 2014.

[17] W. Belardi, "Design and properties of hollow antiresonant fibers for the visible and near infrared spectral range," *IEEE J. Lightwave Technol.*, Vol. 33, No. 21, pp. 4497–4503, 2015.

[18] A. F. Kosolapov, G. K. Alagashev, A. N. Kolyadin, A. D. Pryamikov, A. S. Biryukov, I. A. Bufetov, and E. M. Dianov, "Hollow-core revolver fibre with a double-capillary reflective cladding," *Quantum Electron.*, Vol. 46, No. 3, pp. 267–270, 2016.

[19] F. Yu and J. C. Knight, "Negative curvature hollow-core optical fiber," *IEEE J. Selected Topics Quantum Electron.*, Vol. 22, No. 2, 4400610, 2016.

[20] F. Yu, M. Xu, and J. C. Knight, "Experimental study of low-loss single-mode performance in anti-resonant hollow-core fibers," *Opt. Express*, Vol. 24, No. 12, pp. 12969–12975, 2016.

[21] Y. Wang and W. Ding, "Confinement loss in hollow-core negative curvature fiber: A multi-layered model," *Opt. Express*, Vol. 25, No. 26, pp. 33122–33133, 2017.

[22] B. Debord, A. Amsanpally, M. Chafer, A. Baz, M. Maurel, J. M. Blondy, E. Hugonnot, F. Scol, L. Vincetti, F. Gérôme, and F. Benabid, "Ultralow transmission loss in inhibited-coupling guiding hollow fibers," *Optica*, Vol. 4, No. 2, pp. 209–217, 2017.

[23] C. Wei, R. J. Weiblen, C. R. Menyuk, and J. Hu, "Negative curvature fibers," *Ad. Opt. Photon.*, Vol. 9, No. 3, pp. 504–561, 2017.

[24] I. A. Bufetov, A. F. Kosolapov, A. D. Pryamikov, A. V. Gladyshev, A. N. Kolyadin, A. A. Krylov, Y. P. Yatsenko, and A. S. Biriukov, "Revolver hollow core optical fibers," *Fibers*, Vol. 6, pp. 39-1–39-26, 2018.

[25] T. D. Bradley, J. R. Hayes, Y. Chen, G. T. Jasion, S. R. Sandoghchi, R. Slavik, E. N. Fokoua, S. Bawn, H. Sakr, I. A. Davidson, A. Taranta, J. P. Thomas, M. N. Petrovich, D. J. Richardson, and F. Poletti, "Record low-loss 1.3 dB/km data transmitting antiresonant hollow core fibre," *Proc. Eur. Conf. Opt. Commun. (ECOC 2018)*, TH3F2, pp. 1–3, 2018.

[26] B. Debord, F. Amrani, L. Vincetti, F. Gérôme, and F. Benabid, "Hollow-core fiber technology: the rising of 'gas photonics'," *Fibers*, Vol. 7, pp. 16-1–16-58, 2019.

[27] T. Bradley, J. Hayes, L. Hooper, H. Sakr, G. Jasion, M. Alonso, A. Taranta, A. Saljoghei, M. Fake, I. Davidson, Y. Chen, N. Wheeler, E. Fokoua, W. Wang, S. R. Sandoghchi, D. Richardson, F. Poletti, and H. C. Mulvad, "Hollow core fibre with 0.65 dB/km attenuation across the C and L telecommunication bands," *Proc. Eur. Conf. Opt. Commun. (ECOC 2019)*, PD.3.1, 2019.

[28] F. Yu, P. Song, D. Wu, T. Birks, D. Bird, and J. C. Knight, "Attenuation limit of silica-based hollow-core fiber at mid-IR wavelengths," *Appl. Phys. Lett. Photon.*, Vol. 4, pp. 080803-1–080803-6, 2019.

[29] H. Sakr, Y. Chen, G. T. Jasion, T. D. Bradley, J. R. Hayes, H. C. H. Mulvad, I. A. Davidson, E. N. Fokoua, and F. Poletti, "Hollow core optical fibres with comparable attenuation to silica fibres between 600 and 1100 nm," *Nature Commun.*, Vol. 11, 6030, pp. 1–10, 2020.

[30] G. T. Jasion, T. D. Bradley, K. Harrington, H. Sakr, Y. Chen, E. N. Fokoua, I. A. Davidson, A. Taranta, J. R. Hayes, D. J. Richardson, and F. Poletti, "Hollow core NANF with 0.28 dB/km attenuation in the C and L bands," *Proc. Opt. Fiber Conf. (OFC 2020)*, Th4B.4, 2020.

[31] J. C. Knight, J. Broeng, T. A. Birks, and P. St. J. Russell, "Photonic band gap guidance in optical fibers," *Science*, Vol. 282, pp. 1476–1478, 1998.

[32] P. J. Roberts, F. Couny, H. Sabert, B. J. Mangan, D. P. Williams, L. Farr, M. W. Mason, A. Tomlinson, T. A. Birks, J. C. Knight, and P. St. J. Russell, "Ultimate low loss of hollow-core photonic crystal fibers," *Opt. Express*, Vol. 13, No. 1, pp. 236–244, 2005.

[33] G. Vienne, Y. Xu, C. Jackobsen, H. Deyerl, J. B. Jensen, T. Sorensen, T. P. Hansen, Y. Huang, M. Terrel, R. K. Lee, N. A. Mortensen, J. Broeng,

H. Simonsen, A. Bjarkey, and A. Yariv, "Ultra-large bandwidth hollow-core guiding in all-silica Bragg fibers with nano-supports," *Opt. Express*, Vol. 12, No. 15, pp. 3500–3508, 2004.

[34] R. Yu, Y. Chen, L. Shui, and L. Xiao, "Hollow-core photonic crystal fibers gas sensing," *Sensors*, Vol. 20, pp. 2996-1–2996-27, 2020.

[35] A. V. V. Nampoothiri, A. M. Jones, C. Fourcade-Dutin, C. Mao, N. Dadashzadeh, B. Baumgart, Y. Y. Wang, M. Alharbi, T. Bradley, N. Campbell, F. Benabid, B. R. Washburn, K. L. Corwin, and W. Rudolph, "Hollow-core optical fiber gas lasers (HOFGLAS): a review," *Opt. Mat. Express*, Vol. 2, No. 7, pp. 948–961, 2012.

[36] A. Benoit, E. Ilinova, B. Beaudou, B. Debord, F. Gerôme, and F. Benabid, "Apectral-temporal dynamics of high power Raman picosecond pulse using H_2-filled kagome HC-PCF," *Opt. Lett.*, Vol. 42, No. 19, pp. 3896–3899, 2017.

[37] L. Cao, S. Gao, Z. Peng, X. Wang, Y. Wang, and P. Wang, "High peak power 2.8 μm Raman laser in a methane-filled negative-curvature fiber," *Opt. Express*, Vol. 26, No. 5, pp. 5609–5615, 2018.

[38] Z. Li, W. Huang, Y. Cui, and Z. Wang, "Efficient mid-infrared cascade Raman source in methane-filled hollow-core fibers operating at 2.8 μm," *Opt. Lett.*, Vol. 43, No. 19, pp. 4671–4674, 2018.

[39] A. V. Gladyshev, A. F. Kosolapov, M. M Khudyakov, Y. P. Yatsenko, A. N. Kolyadin, A. A. Krylov, A. D. Pryamikov, A. S. Biriukov, M. E. Likhachev, I. A. Bufetov, and E. M. Dianov, "2.9, 3.3, and 3.5 μm Raman lasers based on revolver hollow-core silica fiber filled by $^1H_2/D_2$ gas mixture," *IEEE J. Selected Topics Quantum Electron.*, Vol. 24, No. 3, pp. 0903008-1–0903008-8, 2018.

[40] M. S. Astapovich, A. V. Gladyshev, M. M Khudyakov, A. F. Kosolapov, M. E. Likhachev, and I. A. Bufetov, "Watt-level nanosecond 4.42-μm Raman laser based on silica fiber," *IEEE Photon. Technol. Lett.*, Vol. 31, No. 1, pp. 78–81, 2019.

[41] Y. Wang, M. K. Dasa, A. I. Adamu, J. E. Antonio-Lopez, M. S. Habib, R. Amezcua-Correa, O. Bang, and C. Markos, "High pulse energy and quantum efficiency mid-infrared gas Raman fiber laser targeting CO_2 absorption at 4.2 μm," *Opt. Lett.*, Vol. 45, No. 7, pp. 1938–1941, 2020.

[42] A. Gladyshev, Y. Yatsenko, A. Kolyadin, V. Kompanets, and I. Bufetov, "Mid-infrared 10-μJ-level sub-picosecond pulse generation via stimulated Raman scattering in a gas-filled revolver fiber," *Opt. Mat. Express*, Vol. 10, No. 12, pp. 3081–3089, 2020.

[43] B. Beaudou, F. Gerôme, Y. Y. Wang, M. Alharbi, T. D. Bradley, G. Humbert, J. -L. Auguste, J. -M. Blondy, and F. Benabid, "Millijoule laser pulse delivery for spark ignition through kagome hollow-core fiber," *Opt. Lett.*, Vol. 37, No. 9, pp. 1430–1432, 2012.

[44] P. Jaworski, F. Yu, R. R. J. Maier, W. J. Wadsworth, J. C. Knight, J. D. Shephard, and D. P. J. Hand, "Picosecond and nanosecond pulse delivery through a hollow-core negative curvature fiber for micro-machining applications," *Opt. Express*, Vol. 21, No. 19, pp. 22742–22753, 2013.

[45] A. Ulrich, R. R. J. Maier, F. Yu, J. C. Knight, D. P. J. Hand, and J. D. Shephard, "Flexible delivery of Er:YAG radiation at 2.94 μm with negative curvature silica glass fibers: a new solution for minimally invasive surgical procedures," *Biomedical Opt. Express*, Vol. 4, No. 2, pp. 193–205, 2013.

[46] C. Dumitrache, J. Rath, and A. P. Yalin, "High power spark delivery system using hollow core kagome lattice fibers," *Materials*, Vol. 7, pp. 5700–5710, 2014.

[47] M. Michieletto, J. K. Lyngso, C. Jakobsen, J. Lægsgaard, O. Bang, and T. T. Alkeskjold, "Hollow-core fibers for high power pulse delivery," *Opt. Express*, Vol. 24, No. 7, pp. 7103–7119, 2016.

[48] S. Elizer and B. Wedel, "Hollow core optical fibers for industrial ultra short pulse laser beam delivery applications," *Fibers*, Vol. 6, pp. 80-1–80-11, 2018.

[49] X. Zhu, D. Wu, Y. Wang, F. Yu, Q. Li, Y. Qi, J. Knight, S. Chen, and L. Hu, "Delivery of CW laser power up to 300 Watts at 1080 nm by an uncooled low-loss ant-resonant hollow-core fiber," *Opt. Express*, Vol. 29, No. 2, pp. 1492–1501, 2021.

[50] A. N. Kolyadin, A. F. Kosolapov, and I. A. Bufetov, "Optical discharge propagation along hollow-core optical fibres," *Quantum Electron.*, Vol. 48, No. 12, pp. 1138–1142, 2018.

[51] I. A. Bufetov, A. N. Kolyadin, A. F. Kosolapov, V. P. Efremov, and V. E. Fortov, "Catastrophic damage in hollow core optical fibers under high power laser radiation," *Opt. Express*, Vol. 27, No. 13, pp. 18296–18311, 2019.

[52] M. Thiyagarajan and S. Thompson, "Optical breakdown threshold investigation of 1064 nm laser induced air plasma," *J. Appl. Phys.*, Vol. 111, No. 7, pp. 073302-1–073302-8, 2012.

[53] J. Sticker and J. G. Parker, "Experimental investigation of electrical breakdown in nitrogen and oxygen induced by focused laser radiation at 1.064 μ," *J. Appl. Phys.*, Vol. 53, No. 2, pp. 851–855, 1982.

[54] F. Couny, F. Benabid, and P. S. Light, "Large-pitch kagome-structured hollow-core photonic crystal fiber," *Opt. Lett.*, Vol. 31, No. 24, pp. 3574–3576, 2006.

[55] C. R. Giuliano, "Laser-induced damage to transparent dielectric materials," *Appl. Phys. Lett.*, Vol. 5, No. 7, pp. 137–139, 1964.

[56] I. A. Fersman and K. D. Khazov, "Damage of transparent dielectric surfaces by a laser beam," *Sov. Phys. Tech. Phys.*, Vol. 15, pp. 834–838, 1970.

[57] C. R. Giuliano, "Laser-induced damage in transparent dielectrics: The relationship between surface damage and surface plasmas," *IEEE J. Quantum Electron.*, Vol. QE-8, No. 9, pp. 749–754, 1972.

[58] M. D. Crisp, N. L. Boling, and G. Dubé, "Importance of Fresnel reflections in laser surface damage of transparent dielectrics," *Appl. Phys. Lett.*, Vol. 22, No. 8, pp. 364–366, 1972.

[59] N. L. Boling, M. D. Crisp, and G. Dubé, "Laser induced surface damage," *Appl. Opt.*, Vol. 12, No. 4, pp. 650–660, 1973.

[60] N. Bloembergen, "Laser-induced electric breakdown in solids," *IEEE J. Quantum Electron.*, Vol. QE-10, No. 3, pp. 375–386, 1974.

[61] N. Bloembergen, "Role of cracks, pores, and absorbing inclusions on laser induced damage threshold at surfaces of transparent dielectrics," *Appl. Opt.*, Vol. 12, No. 4, pp. 661–664, 1973.

[62] F. Y. Génin, A. Salleo, T. V. Pistor, and L. L. Chase, "Role of light intensification by cracks in optical breakdown on surfaces," *J. Opt. Soc. Am. A*, Vol. 18, No. 10, pp. 2607–2616, 2001.

[63] A. V. Smith and B. T. Do, "Bulk and surface laser damage of silica by picosecond and nanosecond pulses at 1064 nm," *Appl. Opt.*, Vol. 47, No. 26, pp. 4812–4832, 2008.

[64] P. Kaiser, A. R. Tynes, H. W. Astle, A. D. Pearson, W. G. French, R. E. Jaeger, and A. H. Cherin, "Spectral losses of unclad vitreous silica and soda-lime-silicate fibers," *J. Opt. Soc. Am.*, Vol. 63, No. 9, pp. 1141–1148, 1973.

[65] P. C. Schultz, "Optical absorption of the transition elements in vitreous silica," *J. Am. Ceram. Soc.*, Vol. 57, No. 7, pp. 309–313, 1974.

[66] R. W. Hopper and D. R. Uhlmann, "Mechanism of inclusion damage in laser glass," *J. Appl. Phys.*, Vol. 41, No. 10, pp. 4023–4037, 1970.

[67] M. Shoji, *Heat Transfer Textbook*, Appendix F, University of Tokyo Press, Tokyo, 1995.

[68] H. L. Schick, "A thermodynamic analysis of the high-temperature vaporization properties of silica," *Chem. Rev.*, Vol. 60, pp. 331–362, 1960.

[69] H. Hidai, J. Wada, T. Iwamoto, S. Matsusaka, A. Chiba, T. Kishi, and N. Morita, "Experimental and theoretical study on the driving force and glass flow by laser-induced metal sphere migration in glass," *Sci. Rep.*, Vol. 6, 38545, pp. 1–11, 2016.

[70] D. D. Davis, S. C. Mettler, and D. J. DiGiovani, "A comparative evaluation of fiber fuse models," *Proc. Soc. Photo-Opt. Instrum. Eng.*, Vol. 2966, pp. 592–606, 1996.

[71] B. Jensen, "The quantum extension of the Drude-Zener theory in polar semiconductors," *Handbook of Optical Constants of Solids*, Ed. E. D. Palik, Chap. 9, Academic Press Inc., New York, 1985.

[72] M. A. Ordal, L. L. Long, R. J. Bell, S. E. Bell, R. R. Bell, R. W. Alexander, Jr., and C. A. Ward, "Optical properties of metals Al, Co, Cu, Au, Fe, Pb, Ni, Pd, Pt, Ag, Ti, and W in the infrared and far infrared," *Appl. Opt.*, Vol. 22, No. 7, pp. 1099–1119, 1983.

[73] J. Sakai and Y. Suzuki, "Equivalence between in-phase and antiresonant reflection conditions in Bragg fiber and its application to antiresonant reflecting optical waveguide-type fibers," *J. Opt. Soc. Am. B*, Vol. 28, No. 1, pp. 183–192, 2011.

[74] A. Argyros, "Guided modes and loss in Bragg fibres," *Opt. Express*, Vol. 10, No. 24, pp. 1411–1417, 2002.

[75] A. Deng, M. I. Hasan, Y. Wang, and W. Chang, "Analyzing mode index mismatch and field overlap for light guidance in negative-curvature fibres," *Opt. Express*, Vol. 28, No. 19, pp. 27974–27988, 2020.

[76] N. Shibata and T. Edahiro, "Refractive-index dispersion for GeO_2-, P_2O_5- and B_2O_3-doped silica glasses in optical fibers," *Trans. IECE Jpn.*, Vol. E65, No. 3, pp. 166–172, 1982.

[77] R. M. Atkins, P. G. Simpkins, and A. D. Yabon, "Track of a fiber fuse: a Rayleigh instability in optical waveguides," *Opt. Lett.*, Vol. 28, No. 12, pp. 974–976, 2003.

[78] S. Todoroki, *Fiber Fuse: Light-Induced Continuous Breakdown of Silica Glass Optical Fiber*, Chap. 3, NIMS Monographs, Springer, Tokyo, 2014.

[79] S. A. Ramsden and P. Savic, "A radiative detonation model for the development of a laser-induced spark in air," *Nature*, Vol. 203, No. 4951, pp. 1217–1219, 1964.

[80] L. I. Sedov, *Similarity and Dimensional Methods in Mechanics*, Chap. 4, Academic Press, New York, 1959.

[81] W. Ha, Y. Jeong, and K. Oh, "Fiber fuse in hollow optical fibers," *Opt. Lett.*, Vol. 36, No. 9, pp. 1536–1538, 2011.

[82] S. Lee, J. Park, Y. Jeong, H. Jung, and K. Oh, "Guided wave analysis of hollow optical fiber for mode-coupling device applications," *IEEE J. Lightwave Technol.*, Vol. 27, No. 22, pp. 4919–4926, 2009.

[83] Y. Mizuno, N. Hayashi, H. Tanaka, K. Nakamura, and S. Todoroki, "Propagation mechanism of polymer optical fiber fuse," *Sci. Rep.*, Vol. 4, 4800, pp. 1–4, 2014.

[84] F. F. Chen, *Introduction to Plasma Physics and Controlled Fusion*, 2nd Ed., Chap. 3, Plenum Press, New York, 1984.

[85] Y. Shuto, "Evaluation of high-temperature absorption coefficients of ionized gas plasmas on optical fibers," *IEEE Photon. Technol. Lett.*, Vol. 22, No. 3, pp. 134–136, 2010.

[86] *Modern Developments in Fluid Dynamics*, Ed. S. Goldstein, Chap. 7, Dover, New York, 1965.

[87] *Modern Developments in Fluid Dynamics*, Ed. S. Goldstein, Chap. 1, Dover, New York, 1965.

[88] R. Brückner, "Properties and structure of vitreous silica. II," *J. Non-Cryst. Solids*, Vol. 5, pp. 177–216, 1971.

[89] F. P. Incropera and D. P. DeWitt, *Introduction to Heat Transfer*, 4th Ed., Chap 5, John Wiley & Sons, Inc., New York, 2002.

[90] M. Shoji, *Heat Transfer Textbook*, Chap. 4, University of Tokyo Press, Tokyo, 1995.